Aerosol dynamic processes in the Hunga plume in January 2022: Does water vapor accelerate aerosol aging?

Julia Bruckert[1], Simran Chopra[1], Richard Siddans[2,3], Charlotte Wedler[1], and Gholam Ali Hoshyaripour[1]

[1] Institute of Meteorology and Climate Research Tropospheric Research (IMKTRO), Karlsruhe Institute of Technology (KIT), Karlsruhe, Germany
[2] Remote Sensing Group, STFC Rutherford Appleton Laboratory, Chilton, UK
[3] National Centre for Earth Observation, STFC Rutherford Appleton Laboratory, Chilton, UK

Correspondence: Julia Bruckert (julia.bruckert@kit.edu)

Abstract. The 2022 Hunga eruption injected an unprecedented amount of 150 Tg of water vapor into the stratosphere, accelerating SO_2 oxidation and sulfate aerosol formation. Despite releasing less ash than previous eruptions of similar magnitude, the role of ash in the early plume and its rapid removal remains unclear. We performed experiments with the ICOsahedral Nonhydrostatic model with Aerosols and Reactive Tracers (ICON-ART) to better understand the role of water vapor, SO_2
5 and ash emission, aerosol-radiation interaction, and aerosol dynamical processes (nucleation, condensation, coagulation) in the Hunga plume in the first week after the eruption. Furthermore, we compared our results to satellite observations to validate SO_2 oxidation and aerosol dynamical processes. Our results show that about 1.2 Tg SO_2 emission as well as water vapor emission is necessary to explain both the SO_2 column loadings and sulfate aerosol optical depth during the first week after the eruption. Although the model reproduces well the development of SO_2 and sulfate aerosols, the aerosol dynamics alone cannot explain
10 the ash removal after the eruption, as was seen in satellite images. However, some of the ash might not be detected because of the exceptionally strong coating of the ash particles. Both, the strong coating and a doubling of the sulfate effective radii within one week, occur only when the water vapor emission is considered in the chemistry. Furthermore, aerosol-radiation interaction warms the plume and reduces or, depending on the experiments, even reverses the descent of the water vapor plume due to radiative cooling.

15 # 1 Introduction

Volcanic eruptions emit tephra and gases such as water vapor and sulfur dioxide (SO_2) into the atmosphere. Chemical reactions oxidize SO_2 to sulfuric acid (H_2SO_4) and subsequent sulfate production can form secondary aerosol particles. Both directly emitted primary aerosols (such as volcanic ash) as well as secondary aerosol components can interact with radiation (Niemeier et al., 2009; Muser et al., 2020) and clouds (Malavelle et al., 2017; Haghighatnasab et al., 2022) and, thereby, affect weather
20 and climate (Robock, 2000; Timmreck, 2012).

Aerosol-radiation interaction (ARI) leads to a warming and lofting of volcanic plumes (e.g., Muser et al., 2020; Stenchikov et al., 2021), which can increase the lifetime of volcanic aerosols in the plume. The lifetime of aerosols depends, among others, on the size of the particles which can be modified by aerosol dynamical processes (nucleation, condensation, coagulation,

sedimentation). Muser et al. (2020) showed that volcanic ash aging, i.e., a coating of soluble components (mainly sulfate and
water in volcanic plumes) on insoluble aerosols (here ash), leads to a faster removal of the particles from the atmosphere.
Aerosol aging is faster in the troposphere than in the stratosphere most likely due to the higher humidity (Bruckert et al., 2023).
The lifetime of chemical compounds such as SO_2 depends on the oxidation capacity of the surrounding air. Although Sioris
et al. (2016) found that moderate-size eruptions (volcanic explosivity index (VEI) $4-5$) do not provide an effective mechanism
for large-scale hydration of the stratosphere, it has been shown that water vapor can locally change the atmospheric chemistry
by formation of OH (Bekki, 1995; LeGrande et al., 2016) or increase the oxidation rate of SO_2 to sulfate in Pinatubo-size
eruptions (Abdelkader et al., 2023). Furthermore, Zhu et al. (2020) showed that the presence of ash can increase the removal
of SO_2 from the atmosphere by adsorption on the ash surfaces and subsequent sedimentation.

The eruption of the Hunga submarine volcano (20.6°S, 175.4°W) on 15 January 2022 was outstanding in the satellite era.
Never before has an eruption been instrumentally observed with such high water vapor emissions reaching up into the strato-
and mesosphere. Umbrella plume top heights of about 31 km (Gupta et al., 2022) to 40 km with overshooting tops of about
55-57 km (Carr et al., 2022; Proud et al., 2022) were observed by satellite measurements. Observations in the following days
reveal the main transport altitude to be above 25 km (Asher et al., 2023; Taha et al., 2022; Khaykin et al., 2022).

The observed water vapor emission ranges between more than 50 Tg (Vömel et al., 2022) and around 139 - 150 Tg (Millán
et al., 2022; Xu et al., 2022; Khaykin et al., 2022), which is approximately 10% of the stratospheric water vapor burden. Carn
et al. (2022) estimated an SO_2 emission of about 0.4-0.5 Tg. However, Sellitto et al. (2022) investigated satellite observations
of the first days after the eruption and reported a maximum in the SO_2 burden of about 1.0 Tg on 18 January 2022, three days
after the eruption. They argued that the instruments might have been saturated in the first days of the eruption and/or that ash
and ice covered parts of the SO_2 plume.

Both modeling and observation studies show an exceptionally fast oxidation of SO_2 probably due to the large co-emission
of water vapor (Zhu et al., 2022; Asher et al., 2023), which leads to a quick formation of sulfate aerosols (Sellitto et al., 2022;
Zhu et al., 2022). The derived e-folding times range between 6 and 15 days (6 days in Carn et al. (2022), 12 days in Zhu et al.
(2022); Asher et al. (2023), 15 days in Sellitto et al. (2022)). Asher et al. (2023) estimated from balloon-borne instrumentations
that the sulfate formation was complete within the first three weeks after the eruption, i.e., the conversion of SO_2 was about
three times faster than expected under climatological stratospheric conditions.

Aerosol dynamical processes modify the radius of aerosol particles. For instance, nucleation and sedimentation reduce the
median radius of an aerosol distribution, whereas coagulation and condensation increase the median radius. Boichu et al. (2023)
investigated aerosol data from 20 AERONET stations. Their evaluation show a doubling of the radius within the first week
after the eruption (peak radius of 0.22-0.26 μm one day after the eruption to 0.4-0.5 μm about one week after the eruption).
Asher et al. (2023) measured an effective diameter of up to 1.5 μm (mode median effective diameter at 560 nm) during their
measurement campaign at Réunion island 7-10 days after the eruption.

Satellite observations revealed the presence of ash and ice in the early eruption plume, but these components seem to be
quickly removed from the dispersing plume, as for instance revealed from CALIPSO (Cloud–Aerosol Lidar and Infrared
Pathfinder Satellite Observation) and HIMAWARI-8 data (e.g., Sellitto et al., 2022; Legras et al., 2022; Khaykin et al., 2022).

However, Boichu et al. (2023) found an indication of coated ash particles one week after the eruption (poorly absorbing coarse particles with an effective radius of 4.6 μm), which would appear as spherical particles in satellite products such as CALIOP. Kloss et al. (2022) also observed absorbing and semi-transparent particles with radii <0.5 μm in balloon flights at La Réunion on 23 and 26 January 2022. They argue that these particles could be either small sulfate-coated ash particles or a thin ash layer below a sulfate aerosol layer. Furthermore, Baron et al. (2023) argued that presence of fine ash, indicated by higher absorption capabilities, could not be ruled out from their lidar measurements.

Accurate modeling of the dispersion and processes in the early stage of volcanic plumes strongly depends on the knowledge of the eruption source parameters (ESPs), i.e. the plume height, the mass eruption rate (MER) of the main plume constituents (ash, SO_2, water vapor), the emission profile (e.g., Scollo et al., 2008; Harvey et al., 2018), and the timing of the eruption phases (Bruckert et al., 2022). Both timing and plume height can be derived from satellite measurements. The MER is often derived from plume heights using one-dimensional (1-D) plume models (e.g., Mastin, 2007; Folch et al., 2016), which require estimates of volcanic conditions such as exit temperature, exit velocity, and exit volatile fraction. The total MER and volcanic source conditions for the Hunga eruption were estimated with the 1D volcanic plume rise model Plumeria (Mastin, 2007) in Mastin et al. (2024). They found that the plume had to consist of 90% steam from the ocean in order to be consistent with the tephra fallout measurements around the volcano.

The Hunga eruption emitted material in multiple eruption phases, which are indicated by several types of instruments and methods (e.g., satellite images (Gupta et al., 2022), ionospheric observations of the total electron content (Astafyeva et al., 2022), damage of seafloor cables (Clare et al., 2023), back-propagation of atmospheric waves (Horváth et al., 2024; Matoza et al., 2022; Podglajen et al., 2022; Wright et al., 2022), tsunami simulations (Purkis et al., 2023)). Although all these instruments and methods come up with slightly different timings due to the measurement types and the fact that explosions and emissions are not necessarily the same, the main agreement relevant for this paper is: two major emissions into the atmosphere occurred between 4 and 5 UTC (Gupta et al., 2022) with a complex eruption sequence of multiple pulses (Astafyeva et al., 2022; Clare et al., 2023; Matoza et al., 2022; Horváth et al., 2024; Podglajen et al., 2022; Purkis et al., 2023; Wright et al., 2022), and a final explosion occurred between 8 and 9 UTC (Gupta et al., 2022; Matoza et al., 2022; Horváth et al., 2024; Podglajen et al., 2022).

In this paper, we investigate aerosol dynamical processes in the early Hunga plume with the aim to answer the following research questions: Can model simulations help to constrain the SO_2 injection into the stratosphere during the Hunga eruption? Can aerosol dynamics including ash and sulfate explain the quick loss of ash on the first day of the eruption? What is the role of emission of water vapor, SO_2 and ash, and of ARI in the evolution of the particle effective radius. This paper is structured as follows: Section 2 introduces the model and its setup used for this study, the experiments, and the observations for the model validation. The results are split into three sections: 1. we analyze the contribution of the emission of SO_2, water vapor, and ash, and ARI to the development of the early Hunga plume (section 3); 2. we validate our results with observations with respect to transport, SO_2 oxidation and sulfate formation (section 4); 3. we investigate the contribution of different in-plume processes (ARI, coagulation, emission of water vapor and ash) to the development of the particle effective radius. Finally, we conclude our results in section 6 and discuss limitations of the model setup.

In this paper, we consistently use the term 'volcanic water vapor' to describe the water vapor released into the stratosphere
95 as a result of the Hunga eruption. While most of this water vapor comes from evaporating ocean water (Mastin et al., 2024)
(external water), the plume can also contain volcanological water vapor and entrained water vapor during its ascent.

2 Data and Methods

In this section, the modeling system as well as the observational data used for validation are described.

2.1 ICON-ART modeling system

100 The ICOsahedral Nonhydrostatic (ICON) model is a weather and climate model, which allows seamless predictions from
local to global scale (Zängl et al., 2015; Heinze et al., 2017; Giorgetta et al., 2018). ICON solves the three-dimensional
nonhydrostatic and compressible Navier-Stokes equations on a triangular icosahedral grid. ICON's submodule ART (Aerosols
and Reactive Trace gases) considers emissions, atmospheric processes, and removal of aerosols and chemical tracers (Rieger
et al., 2015). A detailed description of the ART features used for this study is given in chapter 2.1.2.

2.1.1 Microphysics scheme in ICON

Water vapor undergoes temperature-dependent phase changes in the atmosphere. Here, we used ICON's one-moment micro-
physics scheme considering five water tracers, namely water vapor q_v, cloud water q_c, rain water q_r, cloud ice q_i, and snow q_s.
The phase transition between q_v and q_c is calculated by saturation adjustment, i.e., a parametrization which ensures that vapor
and liquid phase are in equilibrium (Prill et al., 2023). The transfer rates between the other water tracers are calculated with
110 parametrizations which assume non-equilibrium processes (Doms et al., 2018).

Large emissions of water vapor into ICON-ART by e.g., a volcanic eruption such as the Hunga eruption, without using any
temperature adjustments (as assumed by Niemeier et al. (2023)), leads to a quick formation of liquid and solid water, which
was also found in other models (Stenchikov et al., 2021). Nevertheless, the total water mass is conserved in ICON-ART (not
shown).

2.1.2 Chemistry and aerosol processes

We represent the gas-phase oxidation of SO_2 to H_2SO_4 by means of ART's simplified OH-chemistry mechanism, which has
been implemented by Weimer et al. (2017). In this mechanism, the oxidation of chemical species such as CH_4 and SO_2 depends
on the abundance of OH, which is parameterized as a function of water vapor and ozone number concentrations. The ozone
concentration is derived from the stratospheric LINOZ (linearized ozone) scheme by McLinden et al. (2000), where the ozone
120 concentration tendency is linearized with respect to the local ozone mixing ratio, temperature and overhead ozone column
density. The simplified OH-chemistry together with the LINOZ scheme has been applied and validated against observations
for the volcanic plumes of the 2019 Raikoke eruption (Muser et al., 2020; Bruckert et al., 2023) and the 2021 La Soufrière
eruption (Bruckert et al., 2023).

The aerosol dynamics module (AERODYN) in ART considers the formation of sulfate and the aging of particles. The details
125 are described in Muser et al. (2020). We assumed seven log-normal modes, including Aitken mode (as soluble), accumulation
modes (as soluble, insoluble, and mixed), coarse modes (as insoluble and mixed) and a giant (as insoluble) mode.

We emitted volcanic ash into the insoluble modes. By nucleation, H_2SO_4 can form sulfate in the soluble Aitken mode.
Condensation of H_2SO_4 on existing particles and coagulation of particles (inter- and intramodal) lead to growth of particles
and changes in the mixing state. Two mechanisms can shift particles from one mode to another. The first mechanism shifts
130 particles from the soluble Aitken to the soluble accumulation mode if a diameter threshold of 0.03 μm is exceeded. If a mass
fraction of soluble coating on insoluble particles exceeds 5%, the second mechanism shifts particles from the insoluble mode
to the corresponding mixed mode.

The process of coagulation in ICON-ART is based on the parametrization by Riemer (2002) and only includes coagulation
due to Brownian motion. The interaction of ash due to electrostatic forces and the dependence on water (wet aggregation),
135 which is important in very dense plumes (i.e., in the first minutes of volcanic eruptions), are not considered.

In ART, water uptake by aerosol particles is realized by the ISORROPIA II model, which calculates gas-aerosol partitioning
according to thermodynamic equilibrium (Fountoukis and Nenes, 2007). The interaction of aerosols and radiation is described
in Muser et al. (2020).

2.1.3 Volcanic emissions

140 Volcanic emissions in ICON-ART are calculated online with the 1-D volcanic plume rise model FPlume by Folch et al. (2016).
FPlume calculates a total MER based on a given plume height. As input parameters for the plume dynamics, FPlume requires
exit temperature, exit velocity, and exit volatile fraction as well as atmospheric profiles above the vent for pressure, temperature,
specific humidity and density (Folch et al., 2016). Details on the coupling of ICON-ART and FPlume are given in Bruckert
et al. (2022).

145 The coupling of ICON-ART with FPlume has been validated against observations for the 2019 Raikoke eruption (Bruckert
et al., 2022) and the 2021 La Soufrière eruption (Bruckert et al., 2023). Different from previous works, which considered only
ash and SO_2 emissions, we additionally emitted water vapor in this study. We assumed the amount of entrained water to be
small compared to the water vapor injected into the atmosphere due to the Hunga eruption and, therefore, we derived the MER
of water vapor from the product of the total MER (from FPlume) and the exit volatile fraction (FPlume does not distinguish
150 between water vapor and volatiles). In order to avoid FPlume from reading meteorological profiles which are strongly affected
by the emission from the previous time step, we provided averaged profiles from an external file instead of the profiles from
the ICON model at every time step.

The input parameters used for FPlume for the eruption phases are summarized in Table 1. We chose the same values for both
eruption phases, because the uncertainty range of the measurement is large and detailed information on plume dynamics during
155 both phases is lacking. Furthermore, we used a plume top height of 33.7 km, which is in the uncertainty range of observations
of the umbrella plume (e.g., neglecting the overshooting top) (e.g., Gupta et al., 2022) and also ensures that approximately
150 Tg water vapor remains in the stratosphere after the emission (phase-transition depends on temperatures and therefore, the

injection height). In our simulations, about 500 Tg solid and less than 50 Tg liquid hydrometeors enter the stratosphere, which subsequently fall out in the first 1-2 days.

		Phase 1	Phase 2
	plume height	33.7 km	33.7 km
	timing	4.00 - 5.00 UTC	8.00 - 9.00 UTC
Assumptions	exit temperature	$100°C$	$100°C$
	exit velocity	225 m/s	225 m/s
	exit volatile fraction	90%	90%
	MER SO_2 (Reference)	1.67×10^5 kg/s	1.67×10^5 kg/s
Calculated with FPlume	total MER	1.20×10^8 kg/s	1.20×10^8 kg/s
	MER of very fine ash	1.58×10^5 kg/s	1.58×10^5 kg/s
	MER of water vapor	1.08×10^8 kg/s	1.08×10^8 kg/s

Table 1. Summary of the assumptions (top) and FPlume-derived MERs (bottom). The plume heights for the umbrella top heights are from Gupta et al. (2022). The MER of SO_2 was derived from the total mass of 1.2 Tg SO_2 after the eruption (Sellitto et al. (2022, 2024) estimated an emission of more than 1.0 Tg). The values for exit temperature, exit velocity and exit volatile fraction were taken from Plumeria experiments by Mastin et al. (2024)

160 **2.2 Model setup and experiments**

We performed seven experiments to investigate the role of water vapor, ash and aerosol dynamics in the first week after the Hunga eruption. The assumptions for the experiments are summarized in Table 2. For all experiments, we performed global simulations with a horizontal grid spacing of about 40 km (R2B06) and 90 vertical levels, resolving the atmosphere up to a height of 75 km. The simulations are initialized with analysis fields provided by the German Weather Service (Deutscher
165 Wetterdienst (DWD)).

Experiment name	Ash emission	Aerosol-radiation interaction	SO_2 emission	H_2O emission	coagulation
noVolc	no emission	–	no emission	no emission	–
Reference	from FPlume	yes	1.2 Tg	coupled to chemistry	yes
1/3xSO_2	from FPlume	yes	0.4 Tg	coupled to chemistry	yes
noH$_2$Ochem	from FPlume	yes	1.2 Tg	no coupling to chemistry	yes
noAsh	no	yes	1.2 Tg	coupled to chemistry	yes
noARI	from FPlume	no	1.2 Tg	coupled to chemistry	yes
noCoag	from FPlume	yes	1.2 Tg	coupled to chemistry	no

Table 2. Experiments performed for this study.

The first estimate of the SO_2 mass in Carn et al. (2022) was on the order of 0.4-0.5 Tg. We therefore used 0.4 Tg in the experiment 1/3xSO_2, similar to the modeling study by Zhu et al. (2022). However, Sellitto et al. (2022) argued that the measurements might have underestimated the SO_2 concentration on the first day. Based on their analysis, Sellitto et al. (2022) proposed a value of at least 1 Tg SO_2 entering the stratosphere during the eruption. Thus, for the experiments Reference,

170 noH_2Ochem, noARI, noAsh, and noCoag we tripled the SO_2 emission compared to the experiment 1/3xSO_2.

The mass of very fine ash was evenly distributed into the three insoluble modes (accumulation, coarse, and giant mode) with median diameters of 0.8, 2.98 and 11.35 μm, respectively, and a standard deviation of 1.4 (Muser et al., 2020).

The observed umbrella radius was expanding to about 80 km (Carr et al., 2022) at 04:30 UTC. Therefore, we distributed the emissions horizontally into ten cells covering an area of approximately 16000 km^3, which is equivalent to the area covered by

175 a circle of radius of 71 km.

2.3 Observations and Methods

In this study, we used observations from the CALIOP instrument for the validation of the aerosol and hydrometeor transport, Ozone Mapping and Profiler Suite (OMPS) SO_2 column loadings for the validation of SO_2 oxidation and transport, and Infrared Microwave Sounding / Infrared Atmospheric Sounding Interferometer (IMS/IASI) sulfate Aerosol Optical Depth (SAOD) for

180 the validation of the sulfate formation and transport.

2.3.1 CALIOP

The CALIOP instrument aboard the CALIPSO satellite provides high-resolution vertical profiles of aerosols and clouds since May 2016. The measurements are based on the backscattered signal at 532 nm and 1064 nm. Two channels receive orthogonally polarized components of the 532 nm backscattered signal, whereas the 1064 nm backscatter intensity is only received at

185 one channel (Winker et al., 2009). We used total attenuated backscatter (ATB) signals and depolarization ratios at 532 nm from the CALIOP instrument to validate the simulated aerosol plume transport (L1 data version 4.11 downloaded from https://asdc.larc.nasa.gov/data/CALIPSO/LID_L1-Standard-V4-11/2022/01/).

The ICON-ART ATB signals were calculated offline from simulated aerosol mass mixing ratios with the forward operator described in Hoshyaripour et al. (2019) and applied to volcanic plumes in Bruckert et al. (2023). In total, nine CALIPSO

190 overpasses traversed the Hunga plume within the first week after the eruption.

2.3.2 OMPS

We validated the modeled transport and SO_2 oxidation with SO_2 column loadings from the OMPS nadir mapper (NM, data product OMPS_NPP_NMSO2_PCA_L2, downloaded from https://search.earthdata.nasa.gov/search). OMPS is a ultraviolet (UV) satellite sensor on NASA/NOAA's Suomi-National Polar-orbiting Partnership (Suomi-NPP) satellite operating since

195 2011 (Carn et al., 2015). It measures the backscattered UV radiance spectra between 300 to 380 nm wavelength with a spectral

resolution of 1 nm. The instruments provides a daily global coverage, which is achieved with a 2800 km cross-track swath with a nadir pixel size of 50 km x 50 km (Carn et al., 2015).

2.3.3 IMS/IASI

Metop IASI is a nadir viewing infra-red Fourier transform spectrometer on Metop A,B and C which provides spectra at
200   $0.5\,\mathrm{cm}^{-1}$ apodised resolution, sampled every $0.25\,\mathrm{cm}^{-1}$, from 625 to $2760\,\mathrm{cm}^{-1}$ (Blumstein et al., 2004). Spectra are measured with four detectors, each with a circular field of view (FOV) on the ground (at nadir) of approximately 12 km diameter, arranged in a 2 x 2 grid within a 50 x 50 km^2 field-of-regard (FOR). IASI scans to provide 30 FOR (i.e., 120 individual spectra) evenly distributed across a 2200 km wide swath. Metop is in sun-synchronous polar orbit with a local time of descending node crossing of 9:30. It therefore provides almost complete global coverage twice per day at 9:30 and 21:30 local time.

205   The Rutherford Appleton Laboratory (RAL) IMS scheme employs the optimal estimation method (Rodgers, 2000) to jointly retrieve atmospheric and surface parameters from IASI (in combination with the microwave sounders also on Metop) (Siddans, 2023). The scheme uses the RTTOV 12 radiative transfer model (Saunders et al., 2017) to simulate measured spectra including the effects of aerosol. IMS retrieves the optical depth of sulfate aerosol at $1170\,\mathrm{cm}^{-1}$ (8.5 μm) (i.e., at the peak of the sulfate aerosol mid-infrared extinction cross section), making the following assumptions to define the profile shape and optical
210   properties: (1) The aerosol extinction coefficient profile is assumed to have a Gaussian shape which peaks at 20 km altitude, with a 1 km full-width-half maximum. (2) The OPAC (Hess et al., 1998) sulphate droplet ("SUSO") aerosol type, at zero relative humidity is assumed to define the aerosol size distribution and optical properties. IMS sulfate aerosol optical depth has been used in previous studies of the Hunga plume (e.g., Sellitto et al., 2022; Legras et al., 2022; Sellitto et al., 2024). The data is available from the UK Centre for Environmental Data Analysis (CEDA) archive (https://catalogue.ceda.ac.uk/uuid/
215   5aa32fb863a048f0b24c541639cfd990/). Data used here are "L3U" files, i.e., data gridded to 0.25°x0.25° spatial sampling in hourly time intervals.

For the comparison with the IMS/IASI SOAD, the ICON-ART SAOD was calculated offline from the mass concentrations of the two soluble modes and their respective mass extinction coefficients derived from Mie calculations for $1130\,\mathrm{cm}^{-1}$.

2.4 SAL analysis

220   The Structure-Amplitude-Location (SAL) method, developed by Wernli et al. (2008, 2009) for validation of modeled and observed precipitation fields, is applied to validate our modeled SO_2 column loadings and sulfate aerosol optical depth (SAOD) against observations.

The SAL method analyzes the agreement of objects in two-dimensional data fields according to three components: Structure (S), Amplitude (A), and Location (L). S compares modeled and observed normalized objects with respect to their volume. It
225   can have values between -2 (modeled objects are too small and/or too peaked) and 2 (modeled objects are too large and/or too flat). A value of zero indicates a perfect agreement of model and observations with respect to the structure. The evaluation of the domain-averaged relative deviation of the modeled fields from observations is given by the component A. Similar to the S component, A varies between -2 (model underestimates the predicted quantity) and 2 (model overestimates the predicted

quantity) with a perfect agreement if A is zero. The agreement in location is given by the component L and is the sum of two
230 steps: first, the agreement between the forecast and observation in terms of the normalized difference between the centers of
mass is calculated. Second, the average distance between the center of mass of all objects and the individual objects is derived.
Each step can reach values between 0 and 1 so that L in total ranges from 0 to 2 with a perfect forecast with respect to the
location at L = 0 (Wernli et al., 2008, 2009).

For the SAL validation of modeled SO_2 column loadings with observations, we used OMPS data. We applied the OMPS
235 detection threshold of 0.2 DU (Li et al., 2017) on both the observational and modeled data field. As the OMPS data is organized
in overpasses, we mapped the data as follows for the SAL comparison: For every overpass, we first chose the corresponding
ICON-ART output dataset and checked whether the plume is detected in both fields. If yes, we mapped the overpass area
for model and observations onto a 0.25°x0.25° grid. If the plume was detected in the subsequent overpasses as well, we
combined these overpasses into one map. In total, we received seven mapped fields containing the plume in the first week after
240 the eruption for the comparison with OMPS: 16 January, 2-4 UTC; 17 January, 2-5 UTC; 18 January, 1-6 UTC; 19 January,
1-8 UTC; 20 January, 1-9 UTC; 21 January, 0-2 UTC; 21 January, 5-11 UTC.

We performed a similar procedure with ICON-ART SAOD and IMS/IASI SAOD data for the SAL validation of the sulfate
mass. The differences to the procedure with the OMPS SO_2 column loadings data are that the IMS/IASI data is already mapped
to a 0.25°x0.25° grid for each overpasses, and that the background of the SAOD observations is much busier and it is more
245 difficult to distinguish the plume. Therefore, we used a threshold of 0.01 for the SAOD model and observational data and
additionally checked whether the SO_2 Hunga plume was available in the same grid cell in the IASI data. In total, twelve
mapped fields containing the plume were detected: 15 January, 21 UTC; 16 January, 10-12 UTC; 16 January, 21-23 UTC;
17 January, 11-13 UTC; 17 January, 22 UTC - 18 January 2 UTC; 18 January, 11-14 UTC; 19 January, 0-3 UTC; 19 January,
12-16 UTC; 20 January, 1-4 UTC; 20 January, 13-17 UTC; 21 January, 1-4 UTC; and 21 January, 15-17 UTC.

250 3 Drivers of in-plume chemistry and microphysics

In this section, we want to investigate the role of ARI, water vapor and ash emission on the oxidation of SO_2 and the formation
of sulfate aerosols and ash aging.

3.1 Impact of water vapor and SO_2 emissions

Previous works have already shown a faster oxidation of SO_2 in the Hunga plume due to the additional emission of water vapor
255 (e.g., Sellitto et al., 2022; Zhu et al., 2022; Asher et al., 2023). Therefore, we focus on the effects of water vapor emission
and SO_2 amount on the microphysical developments in the first hours of the plume (i.e., focus on the experiments 1/3xSO_2,
noH_2Ochem, Reference) and compare our results to existing studies. Figure 1 shows the temporal mass development of SO_2,
sulfate, the water on aerosols, ash, water vapor, and OH in all experiments (except the noVolc case).

The co-emission of water vapor accelerates the oxidation of SO_2 and the formation of sulfate aerosols (comparing 1/3xSO_2
260 and noH_2Ochem experiments in Figure 1a and b), which agrees with the findings by Zhu et al. (2022). The faster SO_2 oxidation
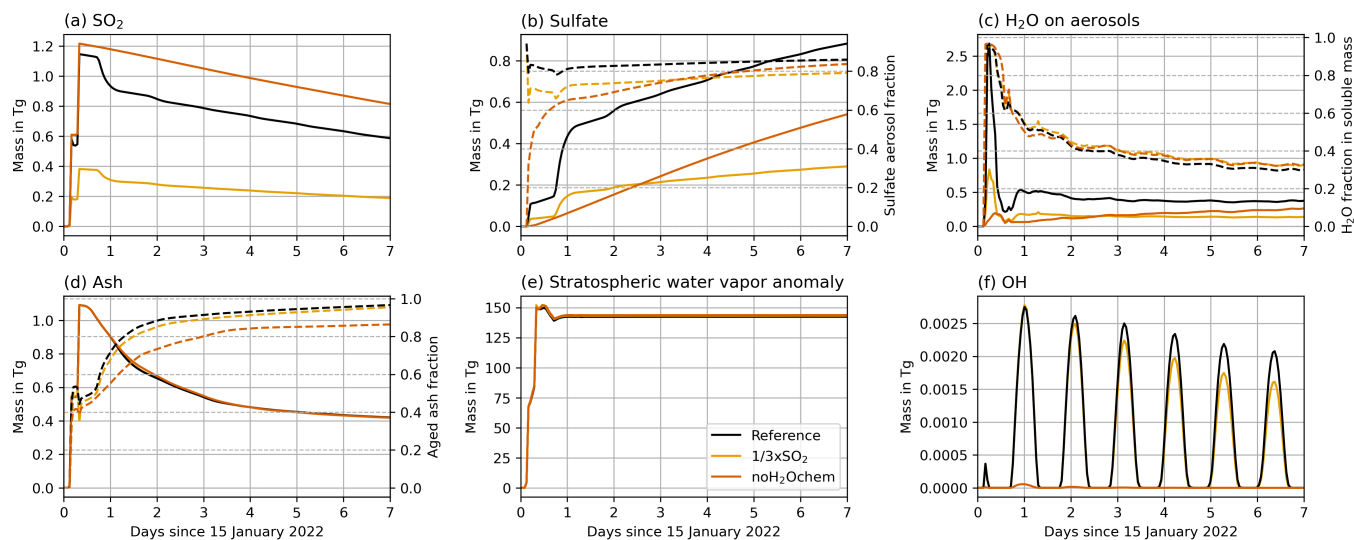
Figure 1. Temporal plume mass development (solid lines, left y-axis) of (a) SO_2, (b) sulfate aerosols plus sulfate on coated ash, (c) liquid water in sulfate aerosols plus liquid water on coated ash, (d) ash, (e) stratospheric water vapor anomaly, and (f) OH for the experiments Reference, 1/3xSO_2, and noH_2Ochem. The dashed lines (right y-axis) indicate fractions of (b) sulfate aerosol mass divided by total sulfate mass, (c) water mass divided by the sum of water and sulfate mass, (d) aged ash mass divided by total ash mass.

in the presence of the water vapor plume is caused by the increase in OH radicals (Figure 1f) as a product of water vapor and ozone chemistry in the stratosphere.

All experiments with H_2O contribution to chemistry show a strong reduction of SO_2 in the last quarter of the first day, whereas, the experiment noH_2Ochem reveals a linear decrease (Fig. 1a) within the first week. This strong decrease is due
265 to both the high water vapor concentration in the plume shortly after the emission and the onset of the OH production by photolysis (Fig. 1a and f).

The experiment with 1/3 SO_2 emission shows a significantly smaller formation of sulfate, because less SO_2 is available for oxidation (Fig. 1a and b). A larger sulfate formation leads to more water accumulation on aerosols (e.g., compare experiments 1/3xSO_2 and Reference in Fig. 1b and c). The H_2O fraction in soluble mass (Fig. 1c, right y-axis) was calculated as the mass
270 of H_2O in aerosols divided by the mass of H_2O and sulfate in aerosols. The fraction peaks during the first hours when the water vapor concentration was highest (i.e., during the emission) and decreases over time. Thus, the fraction of sulfate increases in the soluble mixture. The soluble mass after one week was composed of roughly 2/3 sulfate and 1/3 H_2O with small differences between all experiments including ARI. For experiment noARI, the fraction of H_2O in aerosols is higher (roughly 40%). The reason might be that the plume is transported in lower altitudes in noARI, where the temperatures in the plume are lower and
275 the relative humidity is larger (Figure A1; more on the effect of ARI in section 3.2).

Satellite instruments detected ash on the first day after the eruption, however, it is not detectable in the following days anymore. In the next section, we investigate whether ash played a role on the plume development during the first hours after

the eruption and whether aerosol aging, accelerated by the fast SO_2 oxidation, explains why satellites could not detect ash anymore during the further transport.

3.2 Impact of ash and aerosol-radiation interaction

ARI can increase the scattering of sunlight (e.g., Robock, 2000; Timmreck, 2012) and can reduce photolysis in volcanic plumes. Ash aerosols can coagulate with sulfate or provide surfaces for H_2SO_4 condensation, resulting in the aging of volcanic ash and lower amounts of sulfate aerosols. Here, we first discuss the role of ash and ARI on the development of the Hunga plume. Therefore, we focus on the experiments Reference, noARI, noCoag, and noAsh in Figure 2, i.e., the experiments with larger SO_2 emission.
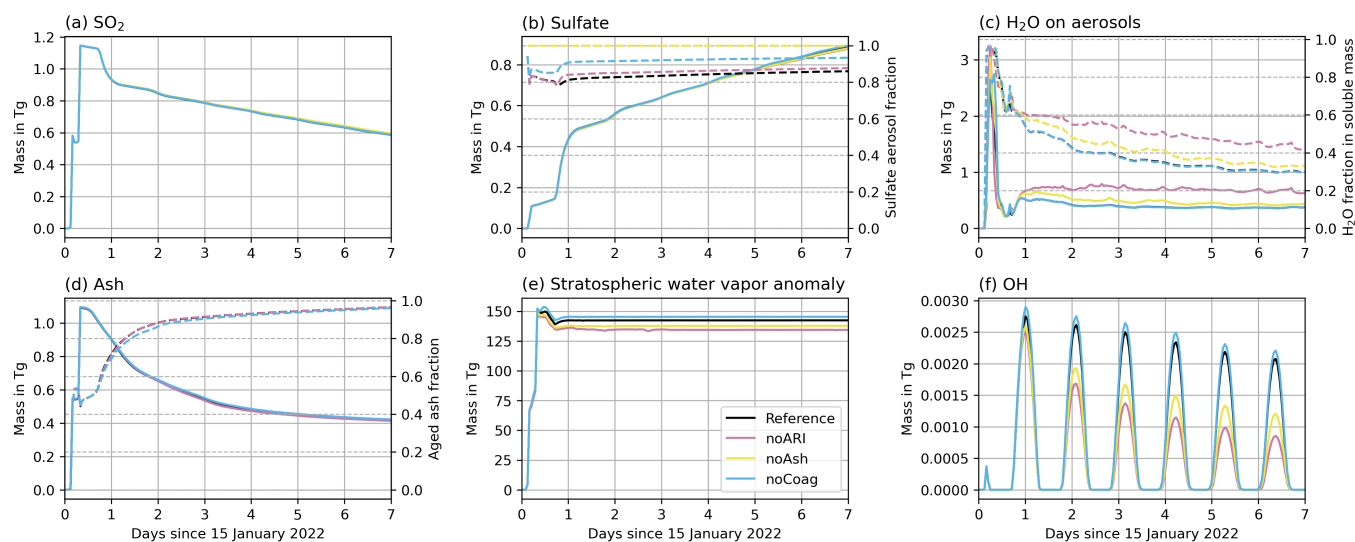
Figure 2. Same as Figure 1, but for the experiments Reference, noARI, noCoag, and noAsh. Note that the curves in a), b), and d) are overlapping.

ARI decreases the oxidation of SO_2 in the Hunga plume only very slightly (Figure 2b, compare noARI and Reference). We note that determining the pure effect of the reduction in sunlight on the SO_2 oxidation is difficult to model in a physically consistent way, because ARI causes a lofting of the plume to layers with larger ozone concentrations. A higher concentration of ozone can increase the SO_2 oxidation, which represents an opposed effect to the reduction of sunlight by ARI, i.e., the pure effect of the blocking of sunlight by aerosols might be larger that the ARI effect visible in Figure 2b.

The presence of ash particles in the plume leads to a slightly lower fraction of sulfate aerosols relative to the total sulfate mass (dashed lines in Figure 2b, compare Reference and noAsh experiments), because ash particles provide surfaces for H_2SO_4 condensation and coagulation. This leads to aging or coating of the ash, which is a bit faster when more SO_2 is emitted (dashed lines in Figure 1d, Reference and 1/3xSO_2 experiment). In all experiments, except the noH$_2$Ochem, more than 90% of the ash mass in the plume is coated after less than 3 days (dashed lines in Figures 1d and 2d). The aging of ash is slower without

H$_2$O contribution to chemistry (Figure 1d dashed line for noH$_2$Ochem). Nevertheless, more than 80% of the ash is aged after one week in the experiment, despite the smaller oxidation of SO$_2$. Comparing the curve for the sulfate aerosol fraction of the noH$_2$Ochem experiment with the curves of the 1/3xSO$_2$, Reference, and noARI experiments, we can conclude that sulfate tends to form a coating on ash particles rather than creating uniform sulfate particles (Figures 1b and 2b). The early aging

300 of ash mainly happens through condensation of soluble components (e.g., sulfate and/or water) rather than coagulation of ash with sulfate aerosols (compare dashed lines for Reference and noCoag in Figure 2d).
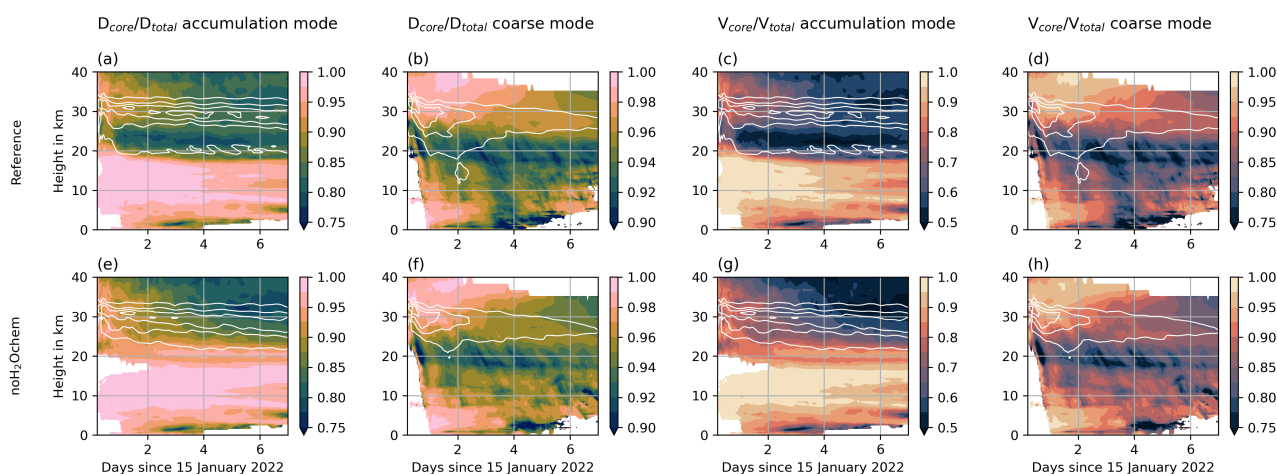
Figure 3. Coating fraction in the Reference experiment (top row) and the noH$_2$Ochem experiment (bottom row) based on the fraction of core to total particle diameter (first and second column) and based on the fraction of core to total particle volume (third and forth column) in color. The first and third column refer to the mixed accumulation mode and the second and forth column refer to the mixed coarse mode. The white contour lines are the normalized masses of the respective mixed mode per m vertical column and indicate the vertical distribution of the plume.

Figure 3 shows the coating fraction with respect to the particle diameter (first and second column) and particle volume (third and fourth column) of the mixed accumulation (first and third column) and the coarse (second and forth column) mode for the Reference (top row) and the noH$_2$Ochem (bottom row) experiment. Besides a larger fraction of aged particles, as discussed

305 before, the coating itself on ash particles also increases with water vapor emission. The differences in coating fraction between the two experiments is largest for the accumulation mode between 20 and 25 km, where the shell makes up about 20% by diameter or about 50% by volume of the particles (compare Figure 3a and e or c and g). For the coarse mode particles, the coating fraction is larger after about three days at the altitude where sedimentation of particles becomes visible, i.e., below 20 km (Figure 3b and f or d and h).

310 Although the aging of ash is faster when large amounts of water vapor are available in the plume, the coating is not large enough to remove majority of the ash within the first day as it was proposed by satellites (e.g. Legras et al., 2022). One reason for the discrepancy between our model results and satellite observations could be that coated ash, which tends to be more spherical compared to the uncoated ash, was interpreted as sulfate by the satellite algorithm. Another reason could be that we

miss one or more important aerosol dynamical processes in our current model setup, such as the coagulation of ash with sea salt
injected into the stratosphere by the eruption. Sea salt is more hygroscopic than sulfate and might increase the water uptake on
aged ash particles, which leads to a faster growth and removal by sedimentation. The neglected activation of ash or the missing
wet aggregation in the plume in our model setup might also explain the discrepancy between our simulations and observations.
However, the role of sea salt in the Hunga plume on aerosol dynamical processes and the effects of aggregation and activation
are beyond the scope of this study and are the topic of another ongoing investigation.

The water vapor development in the plume shows small differences due to aerosol-radiation interaction (Figure 2e, compare
Reference and noARI), which leads to a warming of surrounding air and a lofting of the plume to warmer stratospheric layers
(Muser et al., 2020). However, the amount of ash in the Hunga plume is too small to significantly heat the plume and reduce
the rate of ice formation in the initial phase of the eruption (Figures 1e and 2e). The effect of ARI is discussed in more detail
in the following.
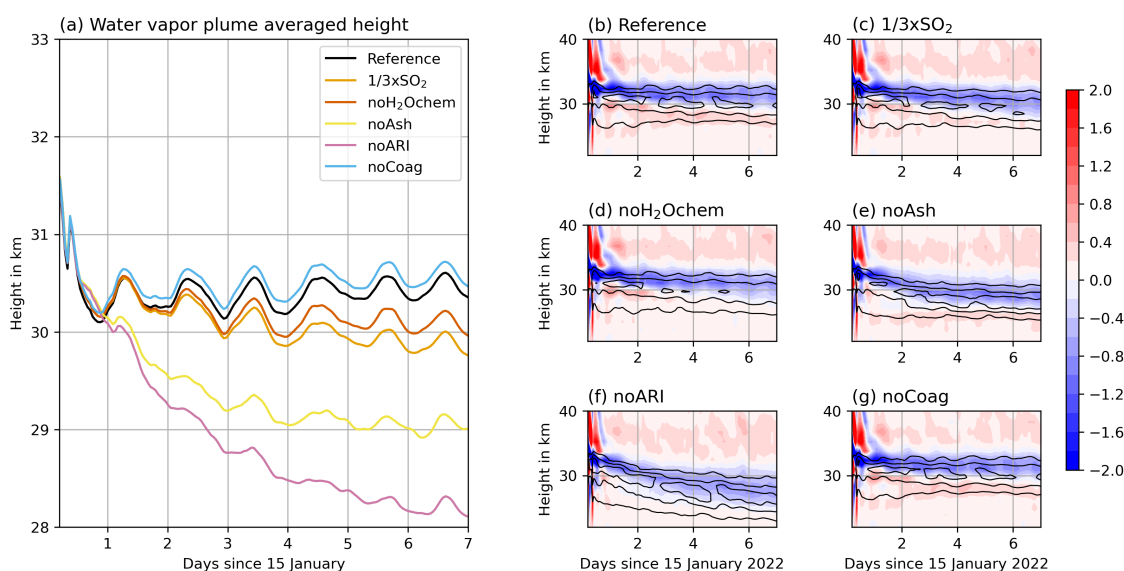
Figure 4. a) Temporal evolution of the mass-averaged water vapor plume height, and b-g) plume temperature anomaly in K in colors and
normalized water vapor mass per m vertical column in black contours for the different experiments.

Figure 4 shows the mass-averaged height of the water vapor plume in the different experiments in a) and the tempera-
ture anomaly of the experiments in b-g). The experiment noARI shows a decrease of more than 3 km within the first week
(Figure 4a) due to water vapor cooling in the stratosphere (Figure 4f). The experiments including ARI also reveal a negative
temperature anomaly from about 28 to 33 km coinciding well with the position of the water vapor plume (Figure 4b-e and g).
However, the descent of the water vapor is reduced (in the noAsh experiment), balanced out (in Reference, noH2Ochem, and
1/3xSO₂ experiments), or even opposed (in the noCoag experiment) after the first day by the warming due to ARI.

All experiments show a steep decrease of the water vapor plume averaged height during the first day (Figure 4a). The reasons are (1) a large concentration of water vapor during and in the first hours after the emission leading to strong radiative cooling, (2) the absence of sunlight during the night (emission at 17.00-18.00 and 21.00-22.00 local time), and (3) the strong formation of sulfate starting after the first day.

The reduction of the descent rate after the first day is due to both sulfate and ash interaction with radiation. Ash contributes by approximately 2/3 (compare Reference and noAsh in Figure 4a) and sulfate contributes by about 1/3 (compare noARI and noAsh in Figure 4a) to the decrease in descent rate.

The experiment noCoag shows the smallest descent rate for the water vapor plume (Figure 4a, blue curve), because coagulation decreases the number concentration of particles and increases the radii. Neglecting this process changes the interaction of aerosols with radiation consequently affecting the plume temperatures and lofting. As smaller particles interact stronger with radiation in the visible range, the warming and lofting of the plume in the noCoag case is larger, which also affects the mass-averaged height of the water vapor plume (Figure 4a and g).

Khaykin et al. (2022) found a descent rate of the plume on the order of 200 m per day during the first three weeks in water vapor observations with the Microwave Limb Sounder (MLS; maximum plume top altitudes decreasing from near 30 km between 16 and 19 January to about 26 km between 1 and 10 February). Together with our finding in noARI, we argue that ARI is necessary to reproduce the observed plume descent. However, our simulations with ash seem to underestimate the ash removal, which leads to an overestimation of the radiative warming by aerosols and an underestimation of the water vapor descent.

Positive temperature anomalies arise in all experiments in the first hours after the eruptions above 33 km (Figure 4b-g). This is an effect of microphysical processes (mainly ice formation) in the plume during the emission (not shown).

4 Validation of model results

In this section, we will only focus on the experiments Reference, noH_2Ochem, and $1/3xSO_2$, as the other experiments show only small differences to the Reference case with respect to the masses of aerosols and SO_2 (section 3). These differences are not distinguishable in the comparison to observations (not shown).

4.1 SAL analysis to validate SO_2 oxidation and sulfate formation

We performed an SAL analysis to validate the modeled SO_2 oxidation with OMPS observations (SO_2 column loadings) and modeled sulfate formation with IMS/IASI observations (SAOD). The results are shown in Figure 5 for the experiments Reference (left), noH_2Ochem (middle), and $1/3xSO_2$ (right).

The best agreement of model and observations with respect to both SO_2 and sulfate is achieved in the Reference simulation (Figure 5a and d). Especially in the latter half of the simulation, all values are close to zero for both SO_2 and sulfate. In the first days, the amplitude value is around 1 for both compounds, which might indicate an overestimation of the variables by
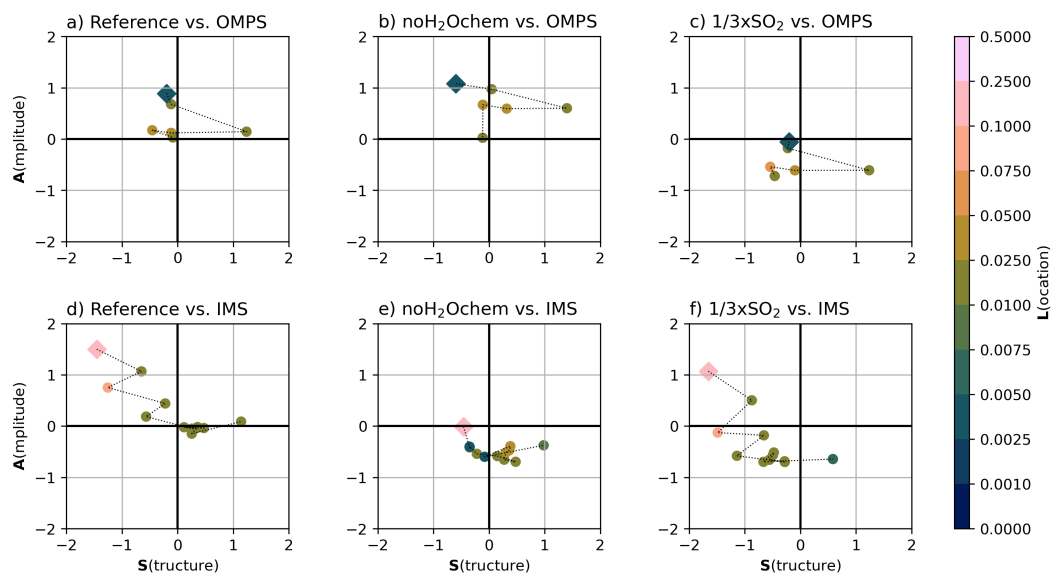
Figure 5. SAL analysis between ICON-ART and OMPS SO_2 column loadings (top, a-c) and between ICON-ART and IMS sulfate AOD (bottom, d-f) for the experiment Reference (left column), noH_2Ochem (middle column), and $1/3xSO_2$ (right column). The structure value is given on the x-axis, the y-axis shows the amplitude value, and the location value is indicated in colours. Each symbol in the plot refers to one comparison date, where the square symbol indicates the first comparison and subsequent comparisons are connected by the dashed line. The corresponding dates are given in section 2.4

the model. However, during the first days a thick ice and ash plume was visible (e.g., Legras et al., 2022), which might have masked SO_2 and sulfate in the observations.

Neglecting the effect of volcanic water vapor on chemistry results in an underestimation of the SO_2 oxidation, i.e., an overes-
365 timation of the SO_2 column loadings (Figure 5b). Additionally, the SAOD and, thus, the sulfate formation was underestimated by the model in the latter half of the simulation in the noH_2Ochem experiment.

Although the $1/3xSO_2$ experiment reveals a reasonable agreement with respect to all SAL components for the SO_2 column loadings in the first half of the simulation, it clearly underestimates the formation of sulfate after the eruption and the SO_2 column loadings in the second half of the simulation (Figure 5c and f). This indicates that the SO_2 mass was larger than the
370 initial estimate of 0.4 Tg by Carn et al. (2022) and was approximately two to three times larger (Sellitto et al., 2022, 2024, and Figure 5a).

The location values for all experiments are slightly better for SO_2 column loadings than for SAOD, because the SO_2 plume can be more distinctly separated from background SO_2 than is the case for sulfate. Nevertheless, the location values indicate a good agreement between model and observations for all times, both components, and all experiments.

4.2 CALIPSO overpasses to validate transport and composition

We analyzed nine Hunga plume overpasses by the CALIPSO satellite and compared the ATB from CALIOP with the Reference, 1/3xSO$_2$, and noH$_2$Ochem experiments as well as the CALIOP depolarization ratio with the spherical fraction ((sulfate mass + aged ash mass) / total aerosol mass) and the sulfate fraction (sulfate mass / total aerosol mass) of the experiments. Figures 6 and 7 show two examples, the other seven overpasses can be found in the Appendix C1-C7.
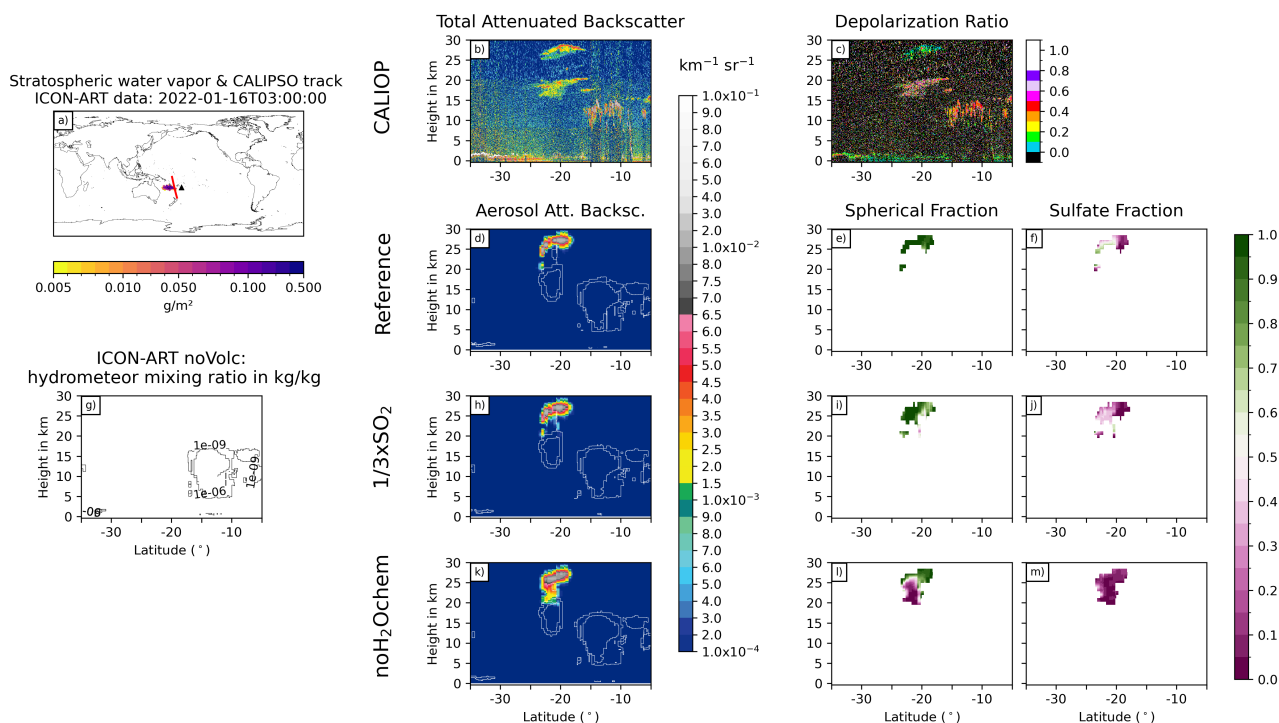
Figure 6. Comparison of ICON-ART and CALIOP for the overpass at 16 January, 2022 at 3 UTC. a) shows the stratospheric water vapor column loadings anomaly from ICON-ART with the CALIPSO track as red line and the location of the volcano as a black triangle. The second column compares CALIOP total ATB at 532 nm (b) to ICON-ART aerosol ATB (in colors) for the experiments Reference (d), 1/3xSO$_2$ (h), and noH$_2$Ochem (k). The white contours refer to the normalized masses of ICON-ART hydrometeors indicating the position of clouds in the model. Panel (g) refers to the mixing ratio of hydrometeors from the simulation noVolc without volcanic eruption in order to distinguish background meteorological clouds from clouds produced by the volcanic emission of water vapor. The third column shows the CALIOP depolarization ratio (c) and ICON-ART fraction of spherical particle mass (mass of sulfate and aged ash divided by total aerosol mass) for the experiments Reference (e), 1/3xSO$_2$ (i), and noH$_2$Ochem (l), respectively. The forth column shows the ICON-ART sulfate fraction defined as the mass of sulfate aerosol divided by the total mass of aerosols for the experiments Reference (f), 1/3xSO$_2$ (j), and noH$_2$Ochem (m), respectively.

The overpass from 16 January 2022 at 3 UTC indicates two plumes at (1) 15-20 km and (2) 27-30 km (20-30 km for noH$_2$Ochem) at about 23 to 27°S, in the CALIOP and ICON-ART ATB (Figure 6b, d, h, k). The upper signal consists of

spherical particles (indicated by the blue-greenish colors in Figure 6c), and it is well reproduced by the aerosol ATB by the ICON-ART experiments Reference and $1/3xSO_2$. The ICON-ART spherical and sulfate fractions of the Reference and $1/3xSO_2$ indicate that this plume is dominated by spherical particles consisting of both aged ash and sulfate (Figure 6e, f, i, and j). For the

385 noH_2Ochem experiment (Figure 6k and i) the upper signal reaches lower altitude and the plume is dominated by non-spherical particles. Thus, without the effect of volcanic water vapor on chemistry the satellite observations can not be reproduced.

The lower signal in the CALIOP ATB most likely originates from ice formed from the Hunga volcanic water vapor, because it is visible in the hydrometeor mixing ratios in all three experiments including volcanic emissions (white contours in Figure 6d, h, and k), but is absent in the experiment without volcanic emission (Figure 6g). The CALIOP depolarization ratio further

390 underlines that this signal comes from non-spherical particles such as ice or uncoated ash (indicated by reddish colors in Figure 6c).

All ICON-ART experiments (with and without volcanic eruption) indicate hydrometeors in the background north of 17°S and their position agrees reasonably well with the position of the signals in the CALIOP total ATB.
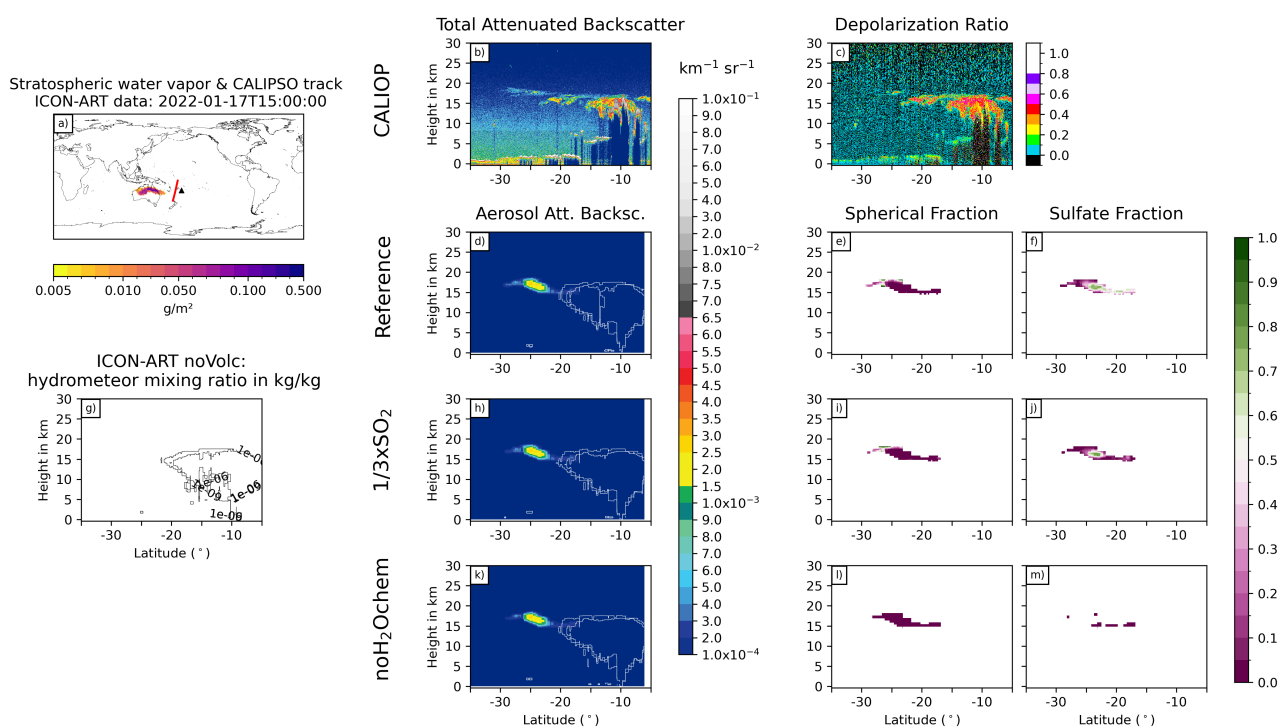
Figure 7. As Fig. 6, but for 17 January, 2022 at 15 UTC

The overpass on 17 January 2022 at 15 UTC shows a layer of non-spherical particles from 5°S to 27°S in the CALIOP

395 measurements at the tropopause (about 18 km), which is only thin at the southern half (less than 3 km thick) and reaches down to 10 km north of 17°S (Figure 7b and c). The northern part most likely arises due to hydrometeors in the background and is visible in all experiments (contour lines in Figure 7d, g, h, and k). The southern part, especially south of 20°S, reveals no

clouds in the ICON-ART experiments but non-spherical aerosol particles (Figure 7d - m). We therefore argue that this signal in the CALIOP total ATB with a rather large depolarization ratio (i.e., non-spherical particles) originates from fresh ash instead
400 of ice clouds. Nevertheless, the amplitude of the aerosol ATB is slightly overestimated by ICON-ART (Figure 7b, d, h, and k).

All in all, the comparison to CALIOP data reveals that parts of the 'missing' ash in satellite data might be hidden due to a strong coating in the presence of volcanic water vapor. However, the simulated aerosol ATB signals tend to overestimate the observed total ATB signals, which agrees with our argumentation in section 3.2 that we miss an important removal processes in our current model setup. Furthermore, the comparison shows that ice particles are present in the plume in model and
405 observations on the first day after the eruption, but the ice was quickly removed, which is in agreement with observations (e.g., Legras et al., 2022; Sellitto et al., 2022).

5 Development of particle sizes

Several measurements show a growth of sulfate particles in the first weeks after the eruption (e.g., Kloss et al., 2022; Asher et al., 2023; Boichu et al., 2023). In this section, we investigate the simulated evolution of the particle size and compare it to
410 previous studies, before we discuss the contribution of the different processes to the particle evolution.

Figure 8 shows height-time cross sections of the sulfate and ash effective radii for the Reference experiment (top row) and deviations from Reference for the noARI, noASH, noH2Ochem, and noCoag experiments. The values are horizontally averaged over the entire plume. The sulfate diameter increases over time during the first week after the eruption by about 2-3 times (Fig. 8a), which has also been found in observations (e.g., Asher et al., 2023; Boichu et al., 2023; Randel et al., 2023).
415 The maximum effective sulfate radius after one week is about 0.35 μm, which is lower than the measured particles sizes of >0.56 μm after seven days in Asher et al. (2023). Boichu et al. (2023) investigated the particle sizes in AERONET data and found an increase of the particle size (peak radius) from 0.22 μm to 0.4-0.5 μm within the first week, which is also larger than our simulated radii. Both studies refer to point measurements instead of plume-averaged values, which might explain the discrepancies of model and observations with respect to the absolute values. As the focus of our work lies on the contribution
420 of aerosol processes to the overall plume development during the first week, a direct comparison with point observations will be addressed in future work.

The ash effective radius decreases fast during the first 2-3 days, because the larger particles sediment faster than smaller ones. After 1 week, ash particles are smaller than 4 μm on average. Boichu et al. (2023) found particles of 5 μm peak radius
425 at one AERONET station and argued that these particles might be sulfate coated ash due to the large size. Our results also indicate that some coated ash might be present in the plume (section 4.2), however, based on the findings in section 3.2, we argue that the total amount is overestimated by the simulations.

The increase of the sulfate effective radius is mainly caused by coagulation of sulfate particles (Fig. 8h) and would be signif-
430 icantly smaller without volcanic water vapor (Figure 8f). The role of coagulation and volcanic water vapor on the development
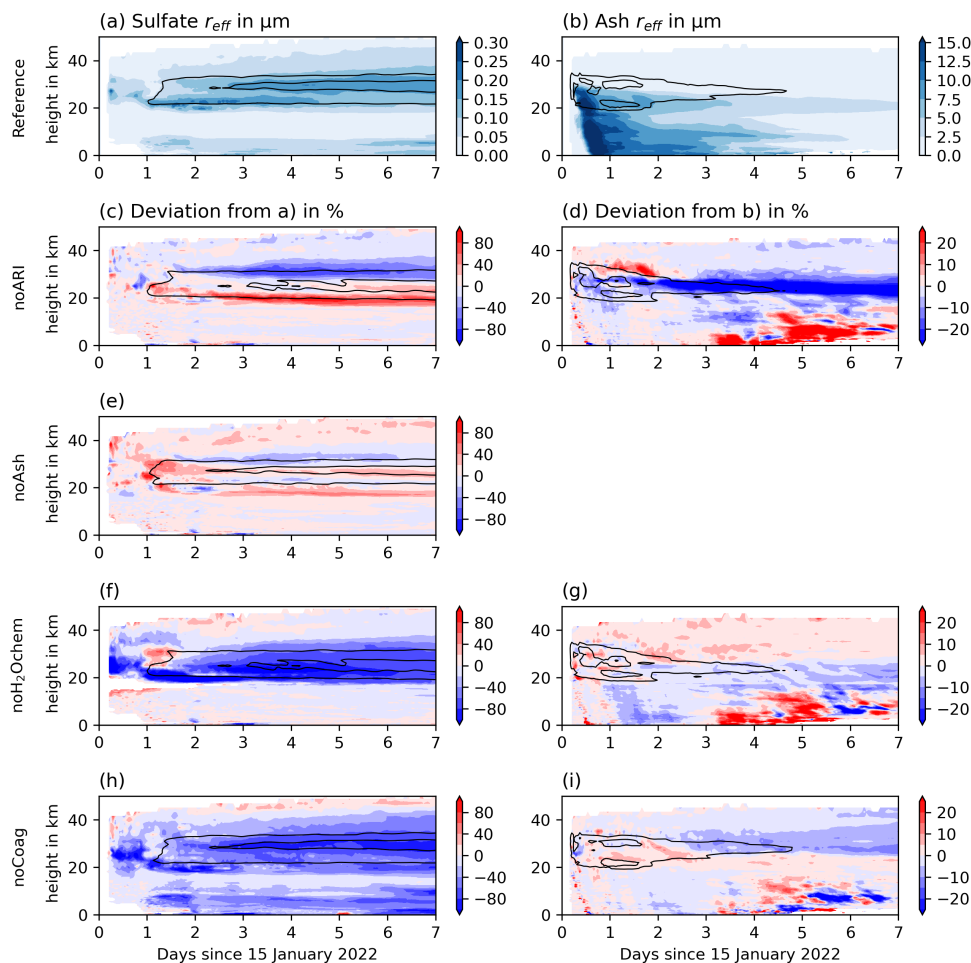
Figure 8. Temporal development of the plume-averaged effective radii for sulfate aerosols (left) and ash aerosols (right) in the Reference experiment (first row), the difference between the experiments noARI and Reference (second row), the experiments noASH and Reference (third row), the experiments noH$_2$Ochem and Reference (forth row), and the experiments noCoag and Reference (fifth row) in colors. The black contour lines indicate the normalized mass of the sulfate (left column) and ash plume (right column) per m vertical column, respectively, in order to visualize the vertical distribution of the plume.

of the ash radius is smaller compared to the sulfate radius evolution (Fig. 8g and i), but still visible. Although we argued in Section 3.1 that ash coagulation with sulfate particles plays a minor role in ash aging, coagulation among ash particles can still contribute to particle growth.

The differences in the effective radii of the noARI and Reference experiment are mainly caused by plume lofting in the
435 Reference case. The radius is smaller at around 30 km and larger at around 20 km already after two days, when ARI is neglected (Fig. 8c). Thus, ARI results in a slower sedimentation of larger particles and an increase of the particle lifetime. This

effect is stronger for ash. Strong negative anomalies are located between 20 and 25 km throughout the entire week, whereas, the radius increases close to the surface after 4.5 days.

When neglecting the emission of ash, the sulfate diameter slightly increases in most altitudes because no sulfate is taken up by ash (Fig. 8e). However, the amplitudes of the anomalies are smaller compared to the noARI experiments. The negative anomaly at around 30 km after 2 days is most likely an effect of aerosol-radiation interaction.

6 Conclusions

We performed a set of experiments with the ICON-ART modeling system to investigate the role of volcanic water vapor on OH chemistry and the role of ash and ARI in the Hunga plume in the first week after the eruption. A validation with OMPS and IASI data reveals a good agreement with respect to transport, SO_2 depletion and sulfate formation for the cases including 1.2 Tg SO_2 and the effect of water vapor emission on chemistry (e.g., Reference experiment). The experiments noH_2Ochem and $1/3xSO_2$ overestimate and underestimate the depletion of SO_2, respectively. Both underestimate the formation of sulfate. Our main findings are:

– Volcanic water vapor accelerates the depletion of SO_2 and formation of sulfate in the Hunga plume which is in agreement with observations (e.g., Legras et al., 2022; Asher et al., 2023) and modeling studies (e.g., Zhu et al., 2022). Additionally, our results show that the volcanic water vapor from the Hunga eruption and the resulting enhancement of the OH-chemistry accelerates ash aging and increases the coating on ash. A comparison with CALIOP data indicates that this effect could mask ash in the observations as spherical particles.

– Aerosol aging due to the processes of condensation and coagulation does not explain the rapid loss of ash after the Hunga eruption as observed by satellite instruments. Although some ash might be masked in the observation due to the strong coating, other important processes are likely missing in our setup that enhance particle growth and removal. Possible limitations could be the coagulation with seasalt and subsequent increase in water vapor accumulation on aerosols, a strong wet aggregation in the early plume (ICON-ART only considers coagulation due to Brownian motion), or the activation of aerosols and subsequent washout.

– Water vapor cools the plume and leads to descent of the water vapor plume. However, this is balanced by the warming of the plume due to ARI. A comparison with observed descent rates indicates that in our simulations with ash emission the warming effect due to aerosols might be overestimated as a result of a missing ash removal process.

– The radius development of the sulfate particles is in agreement with observations with respect to the trend (doubling within one week). Our results show that the process of coagulation as well as the volcanic water vapor effect on chemistry is important to explain the growth of the particles in the first week after the eruption.

Our results are affected by assumptions and uncertainties. The umbrella height of the plume was observed between 30-35 km (Gupta et al., 2022). In our setup, we adjusted the emission height in that way that our stratospheric water vapor anomaly

is in agreement with observations. A larger emission height, however, also goes along with larger concentrations of ozone and OH, which might have effects on the oxidation of SO_2.

470   Bruckert et al. (2022) validated ash column loading for the ICON-ART coupled to FPlume against observations for the 2019 Raikoke eruption and found a good agreement. However, the dynamics of the Hunga eruption are very different compared to the 2019 Raikoke eruption because of the submarine setting of the Hunga volcano. Due to the lack of observations on the ash mass we could not validate our ash emissions in this study. However, the values of the total MER are in agreement with the experiments performed by Mastin et al. (2024) with the Plumeria model (Mastin, 2007) when assuming a plume height of

475   33.7 km.

   Finally, we assumed equal emission strength, height, and length of the two eruption phases as simplifications and due to lacking details. These assumptions lie within the uncertainties of the measurements and observations. Nevertheless, deviations from true values can affect the comparison of the transport, but also microphysical plume processes.

   Despite the limitations and assumptions of our model setup, our findings highlight the role of volcanic water vapor on the

480   aging of particles and the development of sulfate particles as well as the role of ARI on the descent of the Hunga water vapor plume. Although our explains the quick loss of ash particles from the plume only to a certain extent, it contributes to future research on the fate of ash after the Hunga eruption.

Code and data availability.   The ICON and ART models are openly available and accessible through the following link: https://icon-model. org/. Certain code components that are relevant for this work but not open-source conform can be made available upon reasonable request

485   to the corresponding author. The output data from the ICON-ART simulations performed for this study will published at RADAR4KIT after acceptance of the paper.

Author contributions.   JB performed simulations and analyzed the data. CW, GAH, and SC contributed in the discussions of the results. RS prepared and provided the IMS product. JB prepared the paper with significant contributions and comments on the original draft from all authors.

Competing interests.   The authors declare that they have no conflict of interest.

490

Acknowledgements.   This research has been funded by the Deutsche Forschungsgemeinschaft (DFG) as part of the Research Unit VolImpact - subproject VolPlume (FOR2820, DFG Grant 398006378). This work used resources of the Deutsches Klimarechenzentrum (DKRZ) granted by its Scientific Steering Committee (WLA) under project ID bb1070.

References

495   Abdelkader, M., Stenchikov, G., Pozzer, A., Tost, H., and Lelieveld, J.: The effect of ash, water vapor, and heterogeneous chemistry on the evolution of a Pinatubo-size volcanic cloud, Atmospheric Chemistry and Physics, 23, 471–500, https://doi.org/10.5194/acp-23-471-2023, 2023.

Asher, E., Todt, M., Rosenlof, K., Thornberry, T., Gao, R.-S., Taha, G., Walter, P., Alvarez, S., Flynn, J., Davis, S. M., Evan, S., Brioude, J., Metzger, J.-M., Hurst, D. F., Hall, E., and Xiong, K.: Unexpectedly rapid aerosol formation in the Hunga Tonga plume, Proceedings of

500   the National Academy of Sciences, 120, e2219547 120, https://doi.org/10.1073/pnas.2219547120, 2023.

Astafyeva, E., Maletckii, B., Mikesell, T. D., Munaibari, E., Ravanelli, M., Coisson, P., Manta, F., and Rolland, L.: The 15 January 2022 Hunga Tonga Eruption History as Inferred From Ionospheric Observations, Geophysical Research Letters, 49, e2022GL098 827, https://doi.org/https://doi.org/10.1029/2022GL098827, 2022.

Baron, A., Chazette, P., Khaykin, S., Payen, G., Marquestaut, N., Bègue, N., and Duflot, V.: Early Evolution of the Stratospheric Aerosol

505   Plume Following the 2022 Hunga Tonga-Hunga Ha'apai Eruption: Lidar Observations From Reunion (21°S, 55°E), Geophysical Research Letters, 50, e2022GL101 751, https://doi.org/https://doi.org/10.1029/2022GL101751, 2023.

Bekki, S.: Oxidation of volcanic SO2: A sink for stratospheric OH and H2O, Geophysical Research Letters, 22, 913–916, https://doi.org/https://doi.org/10.1029/95GL00534, 1995.

Blumstein, D., Chalon, G., Carlier, T., Buil, C., Hebert, P., Maciaszek, T., Ponce, G., Phulpin, T., Tournier, B., Simeoni, D., Astruc, P., Clauss,

510   A., Kayal, G., and Jegou, R.: IASI instrument: technical overview and measured performances, in: Infrared Spaceborne Remote Sensing XII, vol. 5543, pp. 196 – 207, International Society for Optics and Photonics, SPIE, https://doi.org/10.1117/12.560907, 2004.

Boichu, M., Grandin, R., Blarel, L., Torres, B., Derimian, Y., Goloub, P., Brogniez, C., Chiapello, I., Dubovik, O., Mathurin, T., Pascal, N., Patou, M., and Riedi, J.: Growth and Global Persistence of Stratospheric Sulfate Aerosols From the 2022 Hunga Tonga–Hunga Ha'apai Volcanic Eruption, Journal of Geophysical Research: Atmospheres, 128, e2023JD039 010,

515   https://doi.org/https://doi.org/10.1029/2023JD039010, 2023.

Bruckert, J., Hoshyaripour, G. A., Horváth, A., Muser, L. O., Prata, F. J., Hoose, C., and Vogel, B.: Online treatment of eruption dynamics improves the volcanic ash and SO_2 dispersion forecast: case of the 2019 Raikoke eruption, Atmospheric Chemistry and Physics, 22, 3535–3552, https://doi.org/10.5194/acp-22-3535-2022, 2022.

Bruckert, J., Hirsch, L., Horváth, A., Kahn, R. A., Kölling, T., Muser, L. O., Timmreck, C., Vogel, H., Wallis, S., and Hoshyaripour, G. A.:

520   Dispersion and Aging of Volcanic Aerosols After the La Soufrière Eruption in April 2021, Journal of Geophysical Research: Atmospheres, 128, e2022JD037 694, https://doi.org/https://doi.org/10.1029/2022JD037694, 2023.

Carn, S. A., Yang, K., Prata, A. J., and Krotkov, N. A.: Extending the long-term record of volcanic SO2 emissions with the Ozone Mapping and Profiler Suite nadir mapper, Geophysical Research Letters, 42, 925–932, https://doi.org/https://doi.org/10.1002/2014GL062437, 2015.

Carn, S. A., Krotkov, N. A., Fisher, B. L., and Li, C.: Out of the blue: Volcanic SO2 emissions during the 2021–2022 eruptions of Hunga

525   Tonga—Hunga Ha'apai (Tonga), Frontiers in Earth Science, 10, https://doi.org/10.3389/feart.2022.976962, 2022.

Carr, J. L., Horváth, A., Wu, D. L., and Friberg, M. D.: Stereo Plume Height and Motion Retrievals for the Record-Setting Hunga Tonga-Hunga Ha'apai Eruption of 15 January 2022, Geophysical Research Letters, 49, e2022GL098 131, https://doi.org/https://doi.org/10.1029/2022GL098131, 2022.

Clare, M. A., Yeo, I. A., Watson, S., Wysoczanski, R., Seabrook, S., Mackay, K., Hunt, J. E., Lane, E., Talling, P. J., Pope, E., Cronin,

530   S., Ribó, M., Kula, T., Tappin, D., Henrys, S., de Ronde, C., Urlaub, M., Kutterolf, S., Fonua, S., Panuve, S., Veverka, D., Rapp, R.,

Kamalov, V., and Williams, M.: Fast and destructive density currents created by ocean-entering volcanic eruptions, Science, 381, 1085–1092, https://doi.org/10.1126/science.adi3038, 2023.

Doms, G., Förstner, J., Heise, E., Herzog, H.-J., Mironov, D., Raschendorfer, M., Reinhardt, T., Ritter, B., Schrodin, R., Schulz, J.-P., and Vogel, G.: A Description of the Nonhydrostatic Regional COSMO-Model –Part II: Physical Parameterizations, Deutscher Wetterdienst, https://doi.org/10.5676/DWD_pub/nwv/cosmo-doc_5.05_II, 2018.

Folch, A., Costa, A., and Macedonio, G.: FPLUME-1.0: An integral volcanic plume model accounting for ash aggregation, Geoscientific Model Development, 9, 431–450, https://doi.org/10.5194/gmd-9-431-2016, 2016.

Fountoukis, C. and Nenes, A.: ISORROPIA II: a computationally efficient thermodynamic equilibrium model for $K^+ - Ca^{2+} - Mg^{2+} - NH_4^+ - Na^+ - SO_4^{2-} - NO_3^- - Cl^- - H_2O$ aerosols, Atmospheric Chemistry and Physics, 7, 4639–4659, https://doi.org/10.5194/acp-7-4639-2007, 2007.

Giorgetta, M. A., Brokopf, R., Crueger, T., Esch, M., Fiedler, S., Helmert, J., Hohenegger, C., Kornblueh, L., Köhler, M., Manzini, E., Mauritsen, T., Nam, C., Raddatz, T., Rast, S., Reinert, D., Sakradzija, M., Schmidt, H., Schneck, R., Schnur, R., Silvers, L., Wan, H., Zängl, G., and Stevens, B.: ICON-A, the Atmosphere Component of the ICON Earth System Model: I. Model Description, Journal of Advances in Modeling Earth Systems, 10, 1613–1637, https://doi.org/https://doi.org/10.1029/2017MS001242, 2018.

Gupta, A. K., Bennartz, R., Fauria, K. E., and Mittal, T.: Eruption chronology of the December 2021 to January 2022 Hunga Tonga-Hunga Ha'apai eruption sequence, Communications Earth & Environment, 3, 314, https://doi.org/10.1038/s43247-022-00606-3, 2022.

Haghighatnasab, M., Kretzschmar, J., Block, K., and Quaas, J.: Impact of Holuhraun volcano aerosols on clouds in cloud-system-resolving simulations, Atmospheric Chemistry and Physics, 22, 8457–8472, https://doi.org/10.5194/acp-22-8457-2022, 2022.

Harvey, N. J., Huntley, N., Dacre, H. F., Goldstein, M., Thomson, D., and Webster, H.: Multi-level emulation of a volcanic ash transport and dispersion model to quantify sensitivity to uncertain parameters, Natural Hazards and Earth System Sciences, 18, 41–43, https://doi.org/10.5194/nhess-18-41-2018, 2018.

Heinze, R., Dipankar, A., Henken, C. C., Moseley, C., Sourdeval, O., Trömel, S., Xie, X., Adamidis, P., Ament, F., Baars, H., Barthlott, C., Behrendt, A., Blahak, U., Bley, S., Brdar, S., Brueck, M., Crewell, S., Deneke, H., Di Girolamo, P., Evaristo, R., Fischer, J., Frank, C., Friederichs, P., Göcke, T., Gorges, K., Hande, L., Hanke, M., Hansen, A., Hege, H.-C., Hoose, C., Jahns, T., Kalthoff, N., Klocke, D., Kneifel, S., Knippertz, P., Kuhn, A., van Laar, T., Macke, A., Maurer, V., Mayer, B., Meyer, C. I., Muppa, S. K., Neggers, R. A. J., Orlandi, E., Pantillon, F., Pospichal, B., Röber, N., Scheck, L., Seifert, A., Seifert, P., Senf, F., Siligam, P., Simmer, C., Steinke, S., Stevens, B., Wapler, K., Weniger, M., Wulfmeyer, V., Zängl, G., Zhang, D., and Quaas, J.: Large-eddy simulations over Germany using ICON: a comprehensive evaluation, Quarterly Journal of the Royal Meteorological Society, 143, 69–100, https://doi.org/https://doi.org/10.1002/qj.2947, 2017.

Hess, M., Koepke, P., and Schult, I.: Optical Properties of Aerosols and Clouds: The Software Package OPAC, Bulletin of the American Meteorological Society, 79, 831 – 844, https://doi.org/10.1175/1520-0477(1998)079<0831:OPOAAC>2.0.CO;2, 1998.

Horváth, A., Vadas, S. L., Stephan, C. C., and Buehler, S. A.: One-Minute Resolution GOES-R Observations of Lamb and Gravity Waves Triggered by the Hunga Tonga-Hunga Ha'apai Eruptions on 15 January 2022, Journal of Geophysical Research: Atmospheres, 129, e2023JD039 329, https://doi.org/https://doi.org/10.1029/2023JD039329, 2024.

Hoshyaripour, G. A., Bachmann, V., Förstner, J., Steiner, A., Vogel, H., Wagner, F., Walter, C., and Vogel, B.: Effects of Particle Nonsphericity on Dust Optical Properties in a Forecast System: Implications for Model-Observation Comparison, Journal of Geophysical Research: Atmospheres, 124, 7164–7178, https://doi.org/https://doi.org/10.1029/2018JD030228, 2019.

Khaykin, S., Podglajen, A., Ploeger, F., Grooß, J.-U., Tence, F., Bekki, S., Khlopenkov, K., Bedka, K., Rieger, L., Baron, A., Godin-Beekmann, S., Legras, B., Sellitto, P., Sakai, T., Barnes, J., Uchino, O., Morino, I., Nagai, T., Wing, R., Baumgarten, G., Gerding, M., Duflot, V., Payen, G., Jumelet, J., Querel, R., Liley, B., Bourassa, A., Clouser, B., Feofilov, A., Hauchecorne, A., and Ravetta, F.: Global perturbation of stratospheric water and aerosol burden by Hunga eruption, Communications Earth & Environment, 3, 316, https://doi.org/10.1038/s43247-022-00652-x, 2022.

Kloss, C., Sellitto, P., Renard, J.-B., Baron, A., Bègue, N., Legras, B., Berthet, G., Briaud, E., Carboni, E., Duchamp, C., Duflot, V., Jacquet, P., Marquestaut, N., Metzger, J.-M., Payen, G., Ranaivombola, M., Roberts, T., Siddans, R., and Jégou, F.: Aerosol Characterization of the Stratospheric Plume From the Volcanic Eruption at Hunga Tonga 15 January 2022, Geophysical Research Letters, 49, e2022GL099 394, https://doi.org/https://doi.org/10.1029/2022GL099394, 2022.

LeGrande, A. N., Tsigaridis, K., and Bauer, S. E.: Role of atmospheric chemistry in the climate impacts of stratospheric volcanic injections, Nature Geoscience, 9, 652–655, https://doi.org/10.1038/ngeo2771, 2016.

Legras, B., Duchamp, C., Sellitto, P., Podglajen, A., Carboni, E., Siddans, R., Grooß, J.-U., Khaykin, S., and Ploeger, F.: The evolution and dynamics of the Hunga Tonga–Hunga Ha'apai sulfate aerosol plume in the stratosphere, Atmospheric Chemistry and Physics, 22, 14 957–14 970, https://doi.org/10.5194/acp-22-14957-2022, 2022.

Li, C., Krotkov, N. A., Carn, S., Zhang, Y., Spurr, R. J. D., and Joiner, J.: New-generation NASA Aura Ozone Monitoring Instrument (OMI) volcanic SO_2 dataset: algorithm description, initial results, and continuation with the Suomi-NPP Ozone Mapping and Profiler Suite (OMPS), Atmospheric Measurement Techniques, 10, 445–458, https://doi.org/10.5194/amt-10-445-2017, 2017.

Malavelle, F. F., Haywood, J. M., Jones, A., Gettelman, A., Clarisse, L., Bauduin, S., Allan, R. P., Karset, I. H. H., Kristjánsson, J. E., Oreopoulos, L., Cho, N., Lee, D., Bellouin, N., Boucher, O., Grosvenor, D. P., Carslaw, K. S., Dhomse, S., Mann, G. W., Schmidt, A., Coe, H., Hartley, M. E., Dalvi, M., Hill, A. A., Johnson, B. T., Johnson, C. E., Knight, J. R., O'Connor, F. M., Partridge, D. G., Stier, P., Myhre, G., Platnick, S., Stephens, G. L., Takahashi, H., and Thordarson, T.: Strong constraints on aerosol–cloud interactions from volcanic eruptions, Nature, 546, 485–491, https://doi.org/10.1038/nature22974, 2017.

Mastin, L. G.: A user-friendly one-dimensional model for wet volcanic plumes, Geochemistry, Geophysics, Geosystems, 8, https://doi.org/https://doi.org/10.1029/2006GC001455, 2007.

Mastin, L. G., Van Eaton, A. R., and Cronin, S. J.: Did steam boost the height and growth rate of the giant Hunga eruption plume?, Bulletin of Volcanology, 86, 64, https://doi.org/10.1007/s00445-024-01749-1, 2024.

Matoza, R. S., Fee, D., Assink, J. D., Iezzi, A. M., Green, D. N., Kim, K., Toney, L., Lecocq, T., Krishnamoorthy, S., Lalande, J.-M., Nishida, K., Gee, K. L., Haney, M. M., Ortiz, H. D., Brissaud, Q., Martire, L., Rolland, L., Vergados, P., Nippress, A., Park, J., Shani-Kadmiel, S., Witsil, A., Arrowsmith, S., Caudron, C., Watada, S., Perttu, A. B., Taisne, B., Mialle, P., Pichon, A. L., Vergoz, J., Hupe, P., Blom, P. S., Waxler, R., Angelis, S. D., Snively, J. B., Ringler, A. T., Anthony, R. E., Jolly, A. D., Kilgour, G., Averbuch, G., Ripepe, M., Ichihara, M., Arciniega-Ceballos, A., Astafyeva, E., Ceranna, L., Cevuard, S., Che, I.-Y., Negri, R. D., Ebeling, C. W., Evers, L. G., Franco-Marin, L. E., Gabrielson, T. B., Hafner, K., Harrison, R. G., Komjathy, A., Lacanna, G., Lyons, J., Macpherson, K. A., Marchetti, E., McKee, K. F., Mellors, R. J., Mendo-Pérez, G., Mikesell, T. D., Munaibari, E., Oyola-Merced, M., Park, I., Pilger, C., Ramos, C., Ruiz, M. C., Sabatini, R., Schwaiger, H. F., Tailpied, D., Talmadge, C., Vidot, J., Webster, J., and Wilson, D. C.: Atmospheric waves and global seismoacoustic observations of the January 2022 Hunga eruption, Tonga, Science, 377, 95–100, https://doi.org/10.1126/science.abo7063, 2022.

McLinden, C. A., Olsen, S. C., Hannegan, B., Wild, O., Prather, M. J., and Sundet, J.: Stratospheric ozone in 3-D models: A simple chemistry and the cross-tropopause flux, Journal of Geophysical Research: Atmospheres, 105, 14 653–14 665, https://doi.org/https://doi.org/10.1029/2000JD900124, 2000.

Millán, L., Santee, M. L., Lambert, A., Livesey, N. J., Werner, F., Schwartz, M. J., Pumphrey, H. C., Manney, G. L., Wang, Y., Su, H., Wu, L., Read, W. G., and Froidevaux, L.: The Hunga Tonga-Hunga Ha'apai Hydration of the Stratosphere, Geophysical Research Letters, 49, e2022GL099 381, https://doi.org/https://doi.org/10.1029/2022GL099381, 2022.

Muser, L. O., Hoshyaripour, G. A., Bruckert, J., Horváth, A., Malinina, E., Wallis, S., Prata, F. J., Rozanov, A., von Savigny, C., Vogel, H., and Vogel, B.: Particle aging and aerosol–radiation interaction affect volcanic plume dispersion: evidence from the Raikoke 2019 eruption, Atmospheric Chemistry and Physics, 20, 15 015–15 036, https://doi.org/10.5194/acp-20-15015-2020, 2020.

Niemeier, U., Timmreck, C., Graf, H.-F., Kinne, S., Rast, S., and Self, S.: Initial fate of fine ash and sulfur from large volcanic eruptions, Atmospheric Chemistry and Physics, 9, 9043–9057, https://doi.org/10.5194/acp-9-9043-2009, 2009.

Niemeier, U., Wallis, S., Timmreck, C., van Pham, T., and von Savigny, C.: How the Hunga Tonga—Hunga Ha'apai Water Vapor Cloud Impacts Its Transport Through the Stratosphere: Dynamical and Radiative Effects, Geophysical Research Letters, 50, e2023GL106 482, https://doi.org/https://doi.org/10.1029/2023GL106482, 2023.

Podglajen, A., Le Pichon, A., Garcia, R. F., Gérier, S., Millet, C., Bedka, K., Khlopenkov, K., Khaykin, S., and Hertzog, A.: Stratospheric Balloon Observations of Infrasound Waves From the 15 January 2022 Hunga Eruption, Tonga, Geophysical Research Letters, 49, e2022GL100 833, https://doi.org/https://doi.org/10.1029/2022GL100833, 2022.

Prill, F., Reinert, D., Rieger, D., and Zängl, G.: ICON Tutorial – Working with the ICON Model, Deutscher Wetterdienst, https://doi.org/10.5676/DWD_pub/nwv/icon_tutorial2023, 2023.

Proud, S. R., Prata, A. T., and Schmauß, S.: The January 2022 eruption of Hunga Tonga-Hunga Ha'apai volcano reached the mesosphere, Science, 378, 554–557, https://doi.org/10.1126/science.abo4076, 2022.

Purkis, S. J., Ward, S. N., Fitzpatrick, N. M., Garvin, J. B., Slayback, D., Cronin, S. J., Palaseanu-Lovejoy, M., and Dempsey, A.: The 2022 Hunga-Tonga megatsunami: Near-field simulation of a once-in-a-century event, Science Advances, 9, eadf5493, https://doi.org/10.1126/sciadv.adf5493, 2023.

Randel, W. J., Johnston, B. R., Braun, J. J., Sokolovskiy, S., Vömel, H., Podglajen, A., and Legras, B.: Stratospheric Water Vapor from the Hunga Tonga–Hunga Ha'apai Volcanic Eruption Deduced from COSMIC-2 Radio Occultation, Remote Sensing, 15, https://doi.org/10.3390/rs15082167, 2023.

Rieger, D., Bangert, M., Bischoff-Gauss, I., Förstner, J., Lundgren, K., Reinert, D., Schröter, J., Vogel, H., Zängl, G., Ruhnke, R., and Vogel, B.: ICON-ART 1.0 - A new online-coupled model system from the global to regional scale, Geoscientific Model Development, 8, 1659–1676, https://doi.org/10.5194/gmd-8-1659-2015, 2015.

Riemer, N.: Numerische Simulationen zur Wirkung des Aerosols auf die troposphärische Chemie und die Sichtweite, Ph.D. thesis, https://doi.org/10.5445/IR/2212002, 2002.

Robock, A.: Volcanic Eruptions and Climate, Reviews of Geophysics, 38, 191–219, 2000.

Rodgers, C. D.: Inverse methods for atmospheric sounding: theory and practice, vol. 2, World scientific, 2000.

Saunders, R., Hocking, J., Rundle, D., Rayer, P., Havemann, S., Matricardi, M., Geer, A., Lupu, C., Brunel, P., and Vidot, J.: RTTOV-12 Science and Validation Report, Tech. Rep. Doc ID : NWPSAF-MO-TV-41,Version 1.0, Date : 16/02/2017, 2017.

Scollo, S., Folch, A., and Costa, A.: A parametric and comparative study of different tephra fallout models, Journal of Volcanology and Geothermal Research, 176, 199–211, https://doi.org/10.1016/j.jvolgeores.2008.04.002, 2008.

Sellitto, P., Podglajen, A., Belhadji, R., Boichu, M., Carboni, E., Cuesta, J., Duchamp, C., Kloss, C., Siddans, R., Bègue, N., Blarel, L., Jegou, F., Khaykin, S., Renard, J.-B., and Legras, B.: The unexpected radiative impact of the Hunga Tonga eruption of 15th January 2022, Communications Earth & Environment, 3, 288, https://doi.org/10.1038/s43247-022-00618-z, 2022.

Sellitto, P., Siddans, R., Belhadji, R., Carboni, E., Legras, B., Podglajen, A., Duchamp, C., and Kerridge, B.: Observing the SO2 and Sulfate
645   Aerosol Plumes From the 2022 Hunga Eruption With the Infrared Atmospheric Sounding Interferometer (IASI), Geophysical Research
Letters, 51, e2023GL105 565, https://doi.org/https://doi.org/10.1029/2023GL105565, 2024.

Siddans, R.: Water Vapour CCI: Algorithm Theoretical Basis Document (ATBD) Part 2 - IMS L2 Product version 2.0, Tech. rep., https:
//climate.esa.int/documents/2497/Water_Vapour_CCI_D2.2_ATBD_Part2-IMS_L2_product_v2.0.pdf, 21 November, 2023, 2023.

Sioris, C. E., Zou, J., McElroy, C. T., Boone, C. D., Sheese, P. E., and Bernath, P. F.: Water vapour variability in the high-latitude upper
650   troposphere – Part 2: Impact of volcanic eruptions, Atmospheric Chemistry and Physics, 16, 2207–2219, https://doi.org/10.5194/acp-16-
2207-2016, 2016.

Stenchikov, G., Ukhov, A., Osipov, S., Ahmadov, R., Grell, G., Cady-Pereira, K., Mlawer, E., and Iacono, M.: How Does a Pinatubo-
Size Volcanic Cloud Reach the Middle Stratosphere?, Journal of Geophysical Research: Atmospheres, 126, e2020JD033 829,
https://doi.org/https://doi.org/10.1029/2020JD033829, 2021.

655   Taha, G., Loughman, R., Colarco, P. R., Zhu, T., Thomason, L. W., and Jaross, G.: Tracking the 2022 Hunga Tonga-Hunga Ha'apai Aerosol
Cloud in the Upper and Middle Stratosphere Using Space-Based Observations, Geophysical Research Letters, 49, e2022GL100 091,
https://doi.org/https://doi.org/10.1029/2022GL100091, 2022.

Timmreck, C.: Modeling the climatic effects of large explosive volcanic eruptions, Wiley Interdisciplinary Reviews: Climate Change, 3,
545–564, https://doi.org/10.1002/wcc.192, 2012.

660   Vömel, H., Evan, S., and Tully, M.: Water vapor injection into the stratosphere by Hunga Tonga-Hunga Ha'apai, Science, 377, 1444–1447,
https://doi.org/10.1126/science.abq2299, 2022.

Weimer, M., Schröter, J., Eckstein, J., Deetz, K., Neumaier, M., Fischbeck, G., Hu, L., Millet, D. B., Rieger, D., Vogel, H., Vogel, B.,
Reddmann, T., Kirner, O., Ruhnke, R., and Braesicke, P.: An emission module for ICON-ART 2.0: Implementation and simulations of
acetone, Geoscientific Model Development, 10, 2471–2494, https://doi.org/10.5194/gmd-10-2471-2017, 2017.

665   Wernli, H., Paulat, M., Hagen, M., and Frei, C.: SAL - A Novel Quality Measure for the Verification of Quantitative Precipitation Forecasts,
Monthly Weather Review, 136, 4470 – 4487, https://doi.org/10.1175/2008MWR2415.1, 2008.

Wernli, H., Hofmann, C., and Zimmer, M.: Spatial Forecast Verification Methods Intercomparison Project: Application of the SAL Technique,
Weather and Forecasting, 24, 1472 – 1484, https://doi.org/10.1175/2009WAF2222271.1, 2009.

Winker, D. M., Vaughan, M. A., Omar, A., Hu, Y., Powell, K. A., Liu, Z., Hunt, W. H., and Young, S. A.: Overview of the
670   CALIPSO Mission and CALIOP Data Processing Algorithms, Journal of Atmospheric and Oceanic Technology, 26, 2310 – 2323,
https://doi.org/10.1175/2009JTECHA1281.1, 2009.

Wright, C. J., Hindley, N. P., Alexander, M. J., Barlow, M., Hoffmann, L., Mitchell, C. N., Prata, F., Bouillon, M., Carstens, J., Clerbaux, C.,
Osprey, S. M., Powell, N., Randall, C. E., and Yue, J.: Surface-to-space atmospheric waves from Hunga Tonga–Hunga Ha'apai eruption,
Nature, 609, 741–746, https://doi.org/10.1038/s41586-022-05012-5, 2022.

675   Xu, J., Li, D., Bai, Z., Tao, M., and Bian, J.: Large Amounts of Water Vapor Were Injected into the Stratosphere by the Hunga Tonga–Hunga
Ha'apai Volcano Eruption, Atmosphere, 13, https://doi.org/10.3390/atmos13060912, 2022.

Zängl, G., Reinert, D., Rípodas, P., and Baldauf, M.: The ICON (ICOsahedral Non-hydrostatic) modelling framework of DWD and
MPI-M: Description of the non-hydrostatic dynamical core, Quarterly Journal of the Royal Meteorological Society, 141, 563–579,
https://doi.org/10.1002/qj.2378, 2015.

680   Zhu, Y., Toon, O. B., Jensen, E. J., Bardeen, C. G., Mills, M. J., Tolbert, M. A., Yu, P., and Woods, S.: Persisting volcanic ash particles impact stratospheric SO2 lifetime and aerosol optical properties, Nature Communications, 11, 1–11, https://doi.org/10.1038/s41467-020-18352-5, 2020.

Zhu, Y., Bardeen, C. G., Tilmes, S., Mills, M. J., Wang, X., Harvey, V. L., Taha, G., Kinnison, D., Portmann, R. W., Yu, P., Zosenlof, K. H., Avery, M., Kloss, C., Li, C., Glanville, A. S., Millán, L., Deshler, T., Krotkov, N., and Toon, O. B.: Perturbations in strato-
685   spheric aerosol evolution due to the water-rich plume of the 2022 Hunga-Tonga eruption, Communications Earth & Environment, 3, 248, https://doi.org/10.1038/s43247-022-00580-w, 2022.

Appendix A: Temperature and humidity in aerosol plume
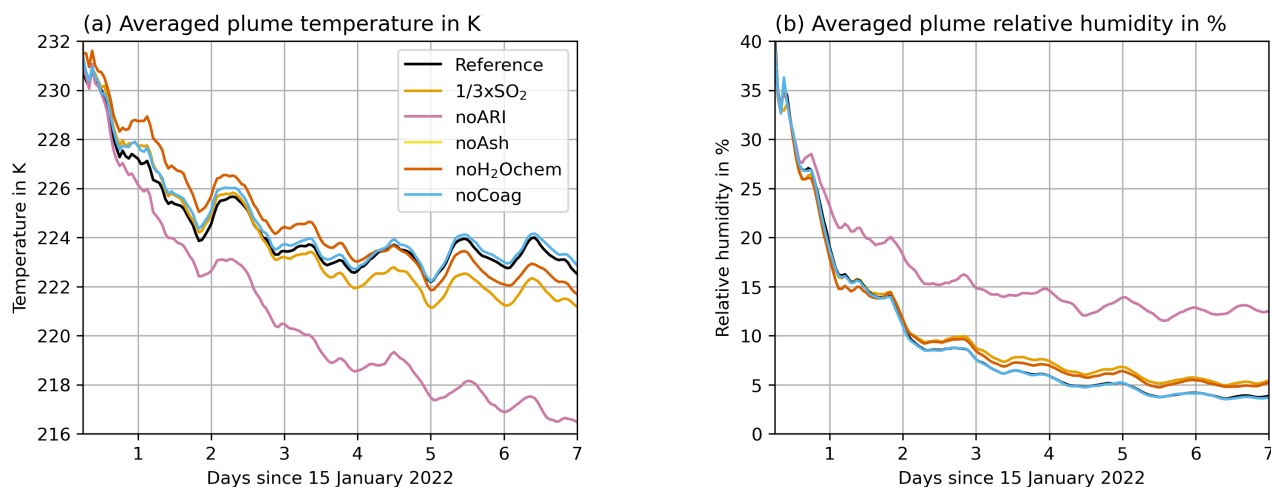
Figure A1. Aerosol-plume averaged a) temperatures in K and b) specific humidity in % in all experiments including the volcanic eruption experiments to explain the difference in the water uptake.

Appendix B: Additional plots for SO₂ and sulfate comparisons
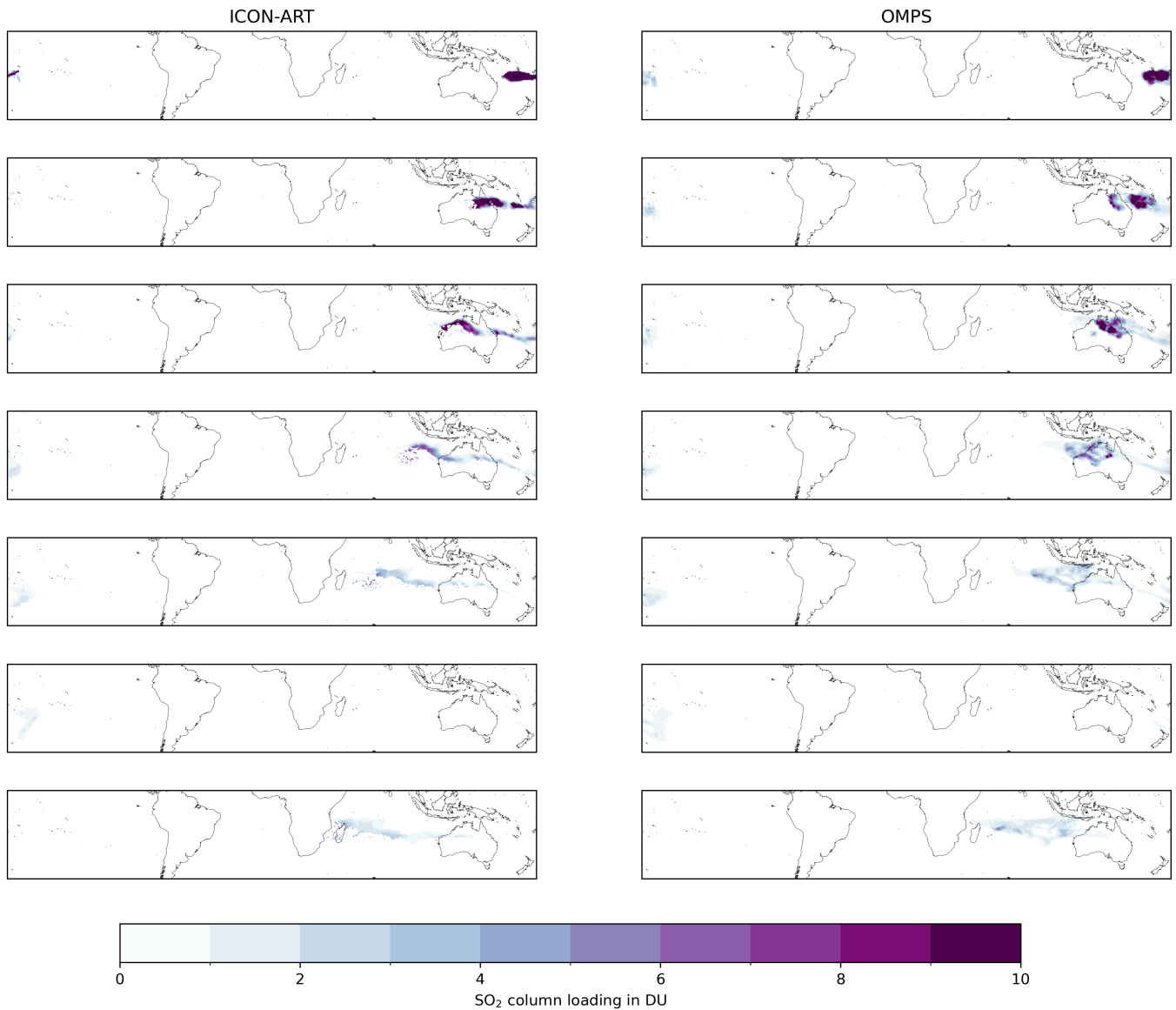
Figure B1. Comparison of the ICON-ART (left) and OMPS (right) SO₂ column loadings in DU for all detected overpasses. The rows from top to bottom refer to the following dates: 16 January, 2-4 UTC; 17 January, 2-5 UTC; 18 January, 1-6 UTC; 19 January, 1-8 UTC; 20 January, 1-9 UTC; 21 January, 0-2 UTC; and 21 January, 5-11 UTC
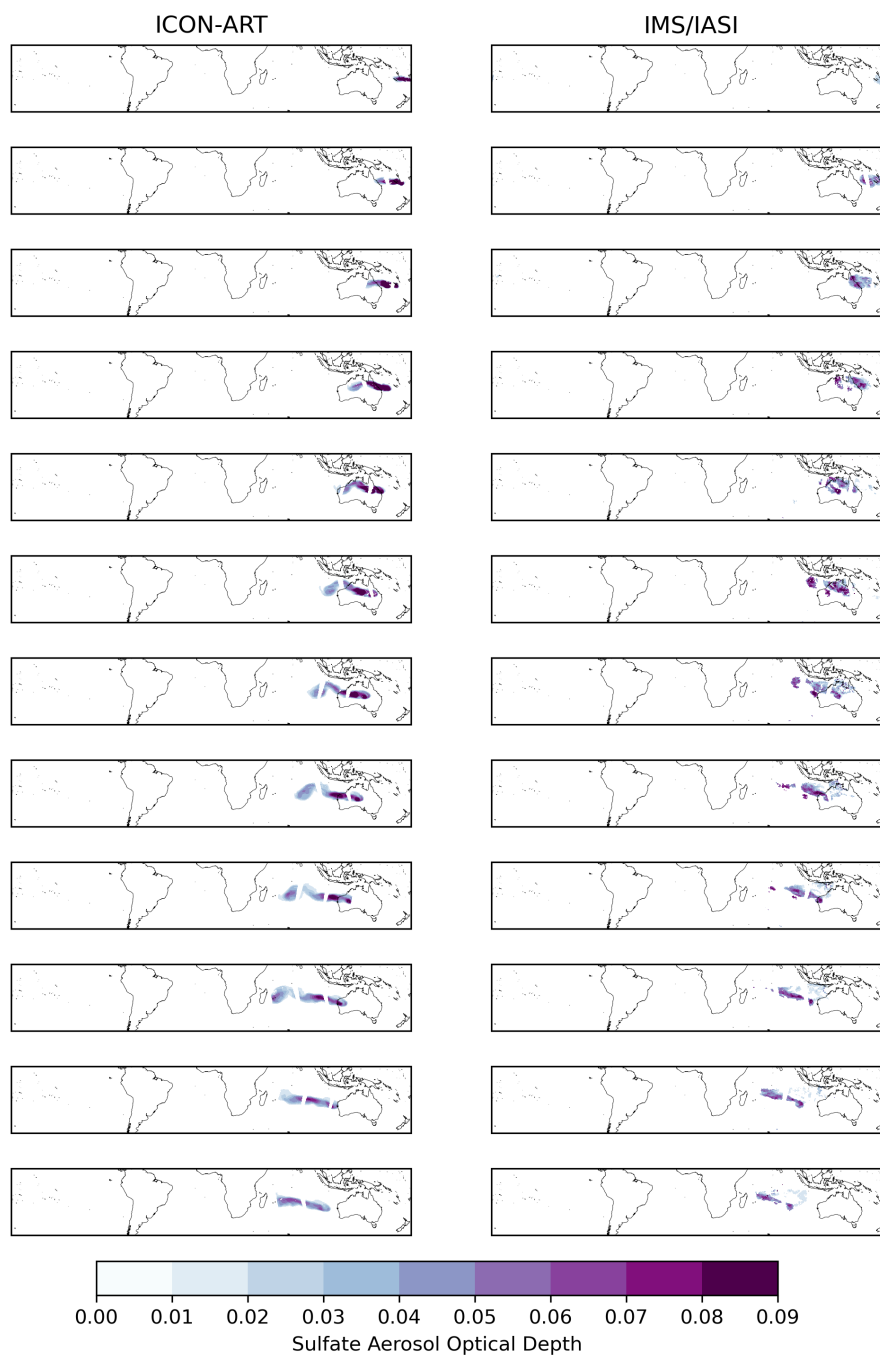
Figure B2. Comparison of the ICON-ART (left) and IMS/IASI (right) SAOD for all detected overpasses. The rows from top to bottom refer to the following dates: 15 January, 21 UTC; 16 January, 10-12 UTC; 16 January, 21-23 UTC; 17 January, 11-13 UTC; 17 January, 22 UTC - 18 January 2 UTC; 18 January, 11-14 UTC; 19 January, 0-3 UTC; 19 January, 12-16 UTC; 20 January, 1-4 UTC; 20 January, 13-17 UTC; 21 January, 1-4 UTC; and 21 January, 15-17 UTC

Appendix C: CALIPSO overpass

Figure C1. As Fig. 6, but for 16 January, 2022 at 16 UTC

Figure C2. As Fig. 6, but for 17 January, 2022 at 16 UTC

Figure C3. As Fig. 6, but for 17 January, 2022 at 18 UTC

Figure C4. As Fig. 6, but for 19 January, 2022 at 7 UTC
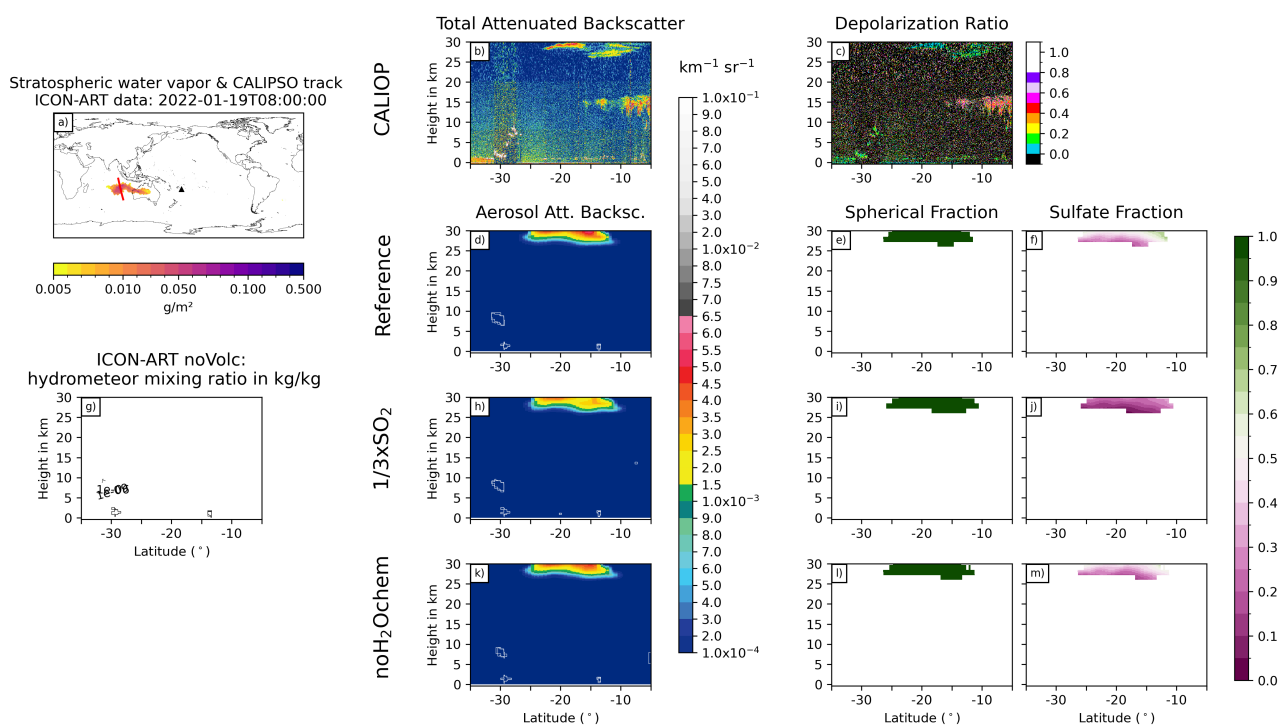
Figure C5. As Fig. 6, but for 19 January, 2022 at 8 UTC

Figure C6. As Fig. 6, but for 19 January, 2022 at 19 UTC

Figure C7. As Fig. 6, but for 19 January, 2022 at 21 UTC